

Topological semimetals and insulators in three-dimensional honeycomb materials

Dennis Wawrzik,¹ David Lindner,¹ Maria Hermanns,^{1,2} and Simon Trebst¹

¹*Institute for Theoretical Physics, University of Cologne, 50937 Cologne, Germany*

²*Department of Physics, University of Gothenburg, SE 412 96 Gothenburg, Sweden*



(Received 15 March 2018; revised manuscript received 29 May 2018; published 10 September 2018)

Semimetals, in which conduction and valence bands touch but do not form Fermi surfaces, have attracted considerable interest for their anomalous properties starting with the discovery of Dirac matter in graphene and other two-dimensional honeycomb materials. Here we introduce a family of three-dimensional honeycomb systems whose electronic band structures exhibit a variety of topological semimetals with Dirac nodal lines. We show that these nodal lines appear in varying numbers and mutual geometries, depending on the underlying lattice structure. They are stabilized, in most cases, by a combination of time-reversal and inversion symmetries and are accompanied by topologically protected “drumhead” surface states. In the bulk, these nodal line systems exhibit Landau level quantization and flat bands upon applying a magnetic field. In the presence of spin-orbit coupling, these topological semimetals are found to generically form (strong) topological insulators. This comprehensive classification of the electronic band structures of three-dimensional honeycomb systems might serve as guidance for future material synthesis.

DOI: [10.1103/PhysRevB.98.115114](https://doi.org/10.1103/PhysRevB.98.115114)

I. INTRODUCTION

In Fermi liquid theory, conventional metals are described by the physics in the vicinity of their Fermi surface. A defining characteristic of a Fermi surface is its codimension of one, which enters, for instance, directly in thermodynamic signatures such as the linear temperature scaling of the specific heat of a metal. Since the early days of solid-state band theory, it has also been known that two bands can accidentally touch each other along manifolds of higher codimension (and thus smaller dimensionality) such as lines or even singular points in momentum space [1]. What has been appreciated only much more recently [2,3] is that in the presence of additional discrete symmetries such as time-reversal, inversion, or certain lattice symmetries, these band touchings can be pinned to the Fermi energy, resulting in semimetals whose nodal structures have codimension two or higher. This insight has paved the way to the recent theoretical prediction and subsequent experimental discoveries of Weyl semimetals [4,5] and nodal-line semimetals [6–9]. Such semimetals exhibit many interesting anomalous properties [9,10] that trace back directly to the nontrivial momentum-space topology of their electronic band structures. As such they are often considered to be gapless cousins of time-reversal invariant topological insulators [11–18].

In this paper, we go back to one of the starting points in the exploration of semimetals—the observation of Dirac points in graphenelike honeycomb materials—and ask whether there is a systematic way to discover novel, nontrivial band structure phenomena by generalizing the underlying honeycomb lattice geometry to three spatial dimensions. Considering the most elementary tricoordinated lattices in three dimensions (discussed in more detail below), we indeed generically find *topological* phenomena in their respective band structures. This includes the formation of Dirac nodal-line semimetals in

lieu of a conventional metal (with a Fermi surface) in many of these systems. Depending on the underlying lattice geometry we find an odd number of nodal lines that remain separated from one another in momentum space, form nodal chains or more complex networks with multiple crossing points, as illustrated in Fig. 1 below. The topological nature of these nodal-line semimetals reveals itself in flat-band surface states, sometimes called drumhead states [6–8], whose origin can be traced back to a nontrivial winding number associated with each nodal line. These nodal-line features are stabilized by discrete symmetries. Recent work, aimed at systematically classifying these symmetries, has identified possible combinations of inversion and time-reversal symmetry (PT) [19–21], sublattice/chiral symmetry [22], crystal reflection [8], non-centrosymmetric [23] and nonsymmorphic lattice symmetries [24] as permissible symmetry sets. Most of our nodal line scenarios are found to comply with the PT -protection mechanism, supplemented by sublattice symmetry which pins the nodal line(s) to the Fermi energy. One exception is found where in the absence of any other symmetries the sublattice symmetry alone suffices to stabilize and pin three nodal lines to the Fermi energy. These nodal-line systems give rise to additional topological band structure phenomena upon applying an external magnetic field or by considering the effect of spin-orbit coupling. In the case of an external magnetic field, one finds a Landau level quantization of extended flat bands in the bulk. In the presence of spin-orbit coupling, the bulk energy spectrum gaps out and the nodal-line semimetals are found to generically transition into (strong) topological insulators.

For some of the three-dimensional honeycomb lattices an alternative scenario plays out with these systems forming conventional metals with a Fermi surface. Upon closer scrutiny, however, some of these systems are found to also exhibit topological bulk and surface features. The nontrivial topology

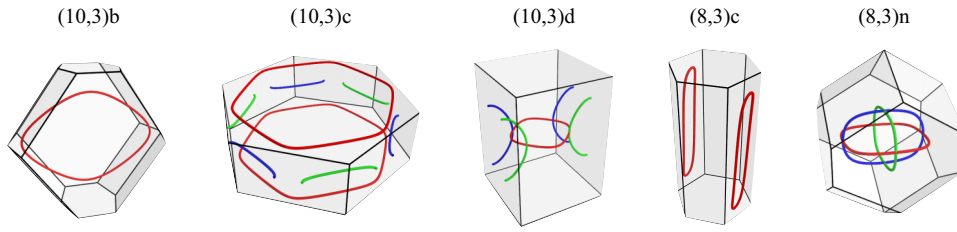


FIG. 1. Overview of nodal line geometries for a set of three-dimensional generalizations of the honeycomb lattice (specified in further detail in Table II). Depending on the underlying lattice geometry one or three nodal lines form that are either separated in momentum space [(10,3)c], form nodal chains [(10,3)d] or complex networks with multiple touching points [(8,3)n].

in these metallic systems arises from Weyl or Dirac cones hidden above/below the Fermi energy, which endows each Fermi surface with a nontrivial Chern number and results in characteristic Fermi arc surface states. For the remaining cases of conventional metals, we find that the inclusion of spin-orbit coupling can lead to nontrivial band-structure phenomena, including the formation of a Dirac semimetal.

Taken all together, our paper presents an exhaustive classification of the electronic band structure phenomena in three-dimensional honeycomb structures. A summary of our results is given in Table I, which indicates for each 3D generalized honeycomb lattice the nodal structure at the Fermi energy for an elementary tight-binding model and in the presence of spin-orbit coupling. This classification provides context to and generalizations of some earlier results obtained for the hyperhoneycomb lattice [25,26] and the hyperoctagon lattice [27]. It also complements a recent classification of Majorana metals in 3D Kitaev spin liquids [28,29] pursued for the same set of 3D generalizations of the honeycomb lattice. We

will comment on analogies and differences of the nodal line physics between the electronic systems considered here and the Majorana metals arising in 3D Kitaev magnets in the discussion at the end of the paper.

The remainder of the paper is structured as follows. We start with an introduction of the 3D honeycomb lattices in Sec. II. Section III is devoted to the physics of topological nodal-line semimetals, which includes a detailed discussion of the underlying symmetry protection, topological surface states, as well as the formation of topological bulk states upon applying an external magnet field or via the inclusion of spin-orbit coupling. Section IV discusses the alternative scenario of a conventional metal forming in some of the 3D honeycomb lattices, putting an emphasis on topological bulk and surface phenomena present also in these systems. We round off our discussion in Sec. V that also touches on the relevance of our study for future material synthesis. Supplementary information is provided in the Appendix.

II. THREE-DIMENSIONAL HONEYCOMB LATTICES

TABLE I. Overview of results. Classification of the nodal structure at the Fermi energy for a number of 3D honeycomb lattices (specified in further detail in Table II). Results for the electronic band structure captured by a tight-binding model are given in the second column. The effect of spin-orbit coupling on the band structure is given in the third column. The last column provides a comparison to the physics of *Majorana* fermions on the same lattices relevant to a family of three-dimensional Kitaev models [28]. The asterisk indicates topological metals where a Weyl/Dirac node is encapsulated by the Fermi surface.

Lattice	Tight binding	Spin-orbit coupling	Kitaev model
(10,3)a	Fermi surface*	Fermi surface*	Fermi surface*
(10,3)b	nodal line	strong TI 1; (000)	nodal line
(10,3)c	3 nodal lines	strong TI 1; (001)	3 nodal lines
(10,3)d	nodal chain	strong TI 1; (000)	nodal chain
(9,3)a	Fermi surface	strong TI 1; (000)	Weyl nodes
(8,3)a	Fermi surface*	Fermi surface*	Fermi surface*
(8,3)b	Fermi surface	$\left\{ \begin{array}{l} \text{weak TI 0; (101)} \\ \text{Dirac nodes} \end{array} \right.$	Weyl nodes
(8,3)c	nodal line	$\left\{ \begin{array}{l} \text{strong TI 1; (010)} \\ \text{Dirac nodes} \end{array} \right.$	nodal line
(8,3)n	3 nodal lines	$\left\{ \begin{array}{l} \text{strong TI 1; (001)} \\ \text{Dirac node} \end{array} \right.$	gapped

The principal input of our study is three-dimensional generalizations of the honeycomb lattice, i.e., lattice structures that, like the familiar honeycomb lattice, exhibit only *tricoordinated* sites. While such low-coordinated lattice structures are relatively rare in conventional solids, they are commonplace in three-dimensional graphene networks [30–32], synthesized as the magnetic sublattice in polymorphs of the iridate Li_2IrO_3 [33,34] and potentially realized in certain metal-organic compounds [35]. Here we take a more abstract point of view and consider a set of *prototypical* tricoordinated lattice structures that contain only elementary loops of identical length. Each one of these lattices is a representative of an entire family of higher harmonics [34] of tricoordinated lattices (where some loops are expanded at the expense of shortening others in a systematic way). The variety of these prototypical lattice structures (with equal loop length) has been extensively classified in pioneering work of A.F. Wells in the 1970s [36]. We provide a summary of these lattices in Table II along with an illustration in Fig. 2. Each lattice is indexed by the Schläfli symbol (p, c) , which indicates the length of the elementary loop p (polygonality) and coordination $c = 3$, followed by a letter. In this notation, the honeycomb lattice would be indexed as (6,3) (not to be followed by a letter as it is the only tricoordinated lattice with loops of length 6). Other familiar lattices include the hyperhoneycomb [33] lattice carrying index (10,3)b and the hyperoctagon [37] lattice (which is also referred to as the Laves graph [38] or K_4 crystal [39] in the

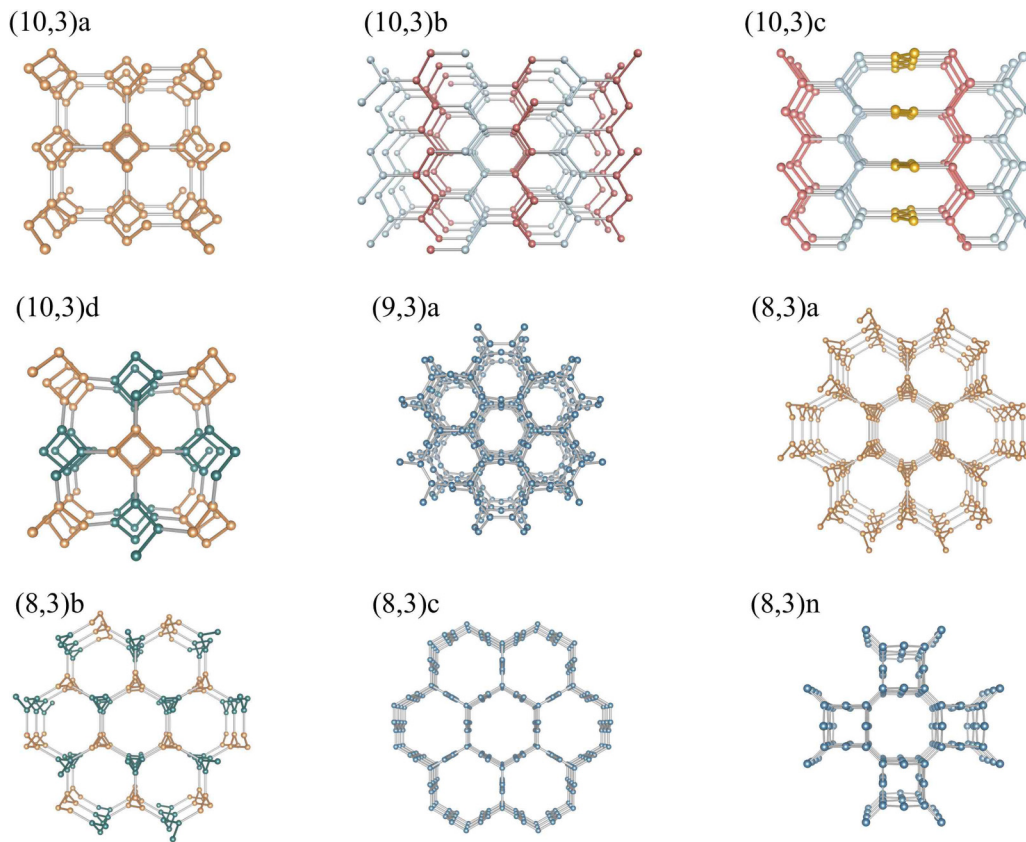


FIG. 2. Illustration of the three-dimensional honeycomb lattices of Table II. Each lattice is labeled by its Schläfli symbol and shown along one of its high-symmetry directions. To highlight important features of the lattice structures, we colored certain bonds/sites: Counterclockwise rotating spirals are marked in orange, while clockwise-rotating ones are blue. For (10,3)b and c, we visualized the different directions of the zigzag bonds using different colors.

literature) that carries index (10,3)a. Beyond their elementary loop length, the prototypical lattices of Table II distinguish themselves by the number of sites in the unit cell (varying

between 4 and 16) and their fundamental lattice symmetries as indicated in the table. Detailed information on all lattices, including their unit cells, lattice and reciprocal lattice vectors is provided in the Appendix.

TABLE II. Overview of three-dimensional honeycomb lattices with tricoordinated sites. The first column gives the Schläfli symbol (p, c) indicating the length of the elementary loop p (polygonality) and coordination $c = 3$ followed by a letter. For each lattice, we provide the number of sites in the unit cell (second column) along with its basic symmetry properties (third and fourth column) and its space group information (last two columns). Further details on the lattice vectors in real and momentum space are provided in Appendix A.

Lattice	Sites in unit cell	Inversion symmetry	Nonsymmorphic	Space group	
				symbol	No.
(10,3)a	4	chiral	✓	$I4_132$	214
(10,3)b	4	✓	✓	$Fddd$	70
(10,3)c	6	chiral	✓	$P3_112$	151
(10,3)d	8	✓	✓	$Pnna$	52
(9,3)a	12	✓		$R\bar{3}m$	166
(8,3)a	6	chiral	✓	$P6_222$	180
(8,3)b	6	✓		$R\bar{3}m$	166
(8,3)c	8	✓	✓	$P6_3/mmc$	194
(8,3)n	16	✓		$I4/mmm$	139

III. NODAL-LINE SEMIMETALS

Probably the most striking topological band structure phenomenon in the three-dimensional honeycomb systems that we consider is the occurrence of Dirac nodal-line semimetals for various lattice geometries. As illustrated in Fig. 1 we find multiple scenarios with varying numbers of nodal lines and mutual geometries. In the following we will discuss various aspects of these nodal-line band structures. We will first concentrate on the elementary symmetry mechanism that leads to the formation of these nodal lines in the (nearest-neighbor) tight-binding Hamiltonian, see Appendix C, and establish that for all but one case it is a combination of time-reversal and inversion symmetry that is at play. The one exception is lattice (10,3)c for which a simple sublattice symmetry suffices. In fact, sublattice symmetry is a crucial symmetry for all lattices as it ensures particle-hole symmetry which in turn pins the nodal line(s) to the Fermi energy. However, if the system is not perfectly particle-hole symmetric (e.g., upon breaking the sublattice symmetry or by moving away from half filling) the nodal line structure will (at least partially) move away from the Fermi energy. We briefly discuss this

instability, which every electronic system clearly exhibits as a sublattice-symmetry breaking next-nearest-neighbor hopping is not symmetry forbidden. We then move to a characterization of the so-called drumhead surface states which accompany the bulk nodal lines and reflect their nontrivial topological character.

Finally, we turn to a discussion of topological bulk phenomena. First, upon applying an external magnetic field one can stabilize flat bands in the bulk that show a characteristic \sqrt{n} Landau level quantization. Last but not least, we will turn to the effect of spin-orbit coupling on the nodal-line semimetals and show that it typically induces a bulk gap and leads to the formation of topological insulators.

A. Symmetry protection

In order to discuss the symmetry mechanism that leads to the formation of nodal lines in our family of three-dimensional honeycomb models, the relevant symmetries are time-reversal symmetry T , inversion symmetry P , sublattice symmetry S , and combinations thereof. Let us first describe the effect of each symmetry individually.

Time-reversal symmetry. Time-reversal symmetry (TRS) is an antiunitary symmetry, which squares to -1 . It relates the energy of an eigenstate with spin- z component σ and momentum \vec{k} to that of a state with spin $-\sigma$ and momentum $-\vec{k}$.

Inversion symmetry. All but three of the lattices we consider here are inversion symmetric (see Table II). Inversion symmetry is a unitary symmetry, which (like time-reversal symmetry) relates energies at \vec{k} and $-\vec{k}$ to each other. Consequently, the combination of inversion and time reversal—in the following denoted by PT —is an antiunitary symmetry that leaves the momentum invariant. Thus, it is a symmetry that is obeyed in the full Brillouin zone. As pointed out in Ref. [21], PT can be used to define a \mathbb{Z}_2 topological invariant that can protect nodal lines.

Sublattice symmetry. With the exception of (9,3)a, all the lattices at hand are bipartite. Therefore, as long as we only consider nearest-neighbor hopping, the resulting Hamiltonian is symmetric under sublattice symmetry. Depending on the lattice details, sublattice symmetry may be implemented in two distinct ways in momentum space: For the lattices (10,3)b, (10,3)c, (10,3)d, (8,3)c, and (8,3)n, both the lattice and the sublattice share the *same* translation vectors, as illustrated in the example of Fig. 3(a). Consequently, one obtains the usual relation,

$$E(\vec{k}) = -E(\vec{k}),$$

namely that for each energy E at momentum \vec{k} there has to be an energy $-E$ at the same momentum \vec{k} . In this realization, the sublattice symmetry imposes the same constraints on the momentum space Hamiltonian as chiral symmetry (i.e., the combination of particle-hole and time-reversal symmetry), which can be used to define a \mathbb{Z}_2 topological invariant that in itself can protect nodal lines [22]. Consequently, the five lattices (10,3)b, (10,3)c, (10,3)d, (8,3)c, and (8,3)n indeed exhibit nodal lines as discussed in the following.

A different implementation of sublattice symmetry is realized for the lattices (10,3)a, (8,3)a, and (8,3)b. Considering a

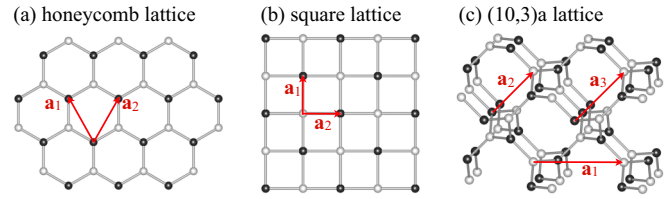


FIG. 3. Illustration of the sublattice symmetry for different lattices. Shown are the A and B sublattices (in white and black, respectively) for the honeycomb, square, and (10,3)a hyperoctagon lattices. While for the honeycomb lattice the two sublattices have the same translation vectors as the original lattice, this does not hold for the other two lattices as at least one of the original lattice translations connects sites of different sublattice types. This leads to a nontrivial translation in momentum space by *half* a reciprocal lattice vector, denoted by a finite value of \vec{k}_0 (see main text).

single sublattice for one of these lattices, one finds that the sublattice has *different* translation vectors than the original lattice, i.e., at least one of the original lattice translations connects sites of different sublattice types. This scenario is illustrated in Figs. 3(b) and 3(c). As a consequence, to implement the sublattice symmetry for these lattices, one needs to artificially enlarge the unit cell of the lattice. This results in a nontrivial translation in momentum space by half a reciprocal lattice vector, denoted by \vec{k}_0 . As a consequence, sublattice symmetry imposes [28] that

$$E(\vec{k}) = -E(\vec{k} + \vec{k}_0),$$

i.e., for each eigenstate with energy E at momentum \vec{k} , there has to be a corresponding one at the shifted momentum $\vec{k} + \vec{k}_0$ with energy $-E$. This second realization of sublattice symmetry does not readily allow us to define a \mathbb{Z}_2 topological invariant that in itself can protect nodal lines. Instead, we find that these lattices generically exhibit an even number of Fermi surfaces, with pairs shifted apart by a momentum \vec{k}_0 as discussed in Sec. IV.

Upon close inspection of all of the aforementioned symmetries for all lattices at hand, we find that in four cases—lattices (10,3)b, (10,3)d, (8,3)c, and (8,3)n—the nodal lines are protected by PT symmetry. In one case, lattice (10,3)c, it is only sublattice symmetry S that protects the nodal line(s). This is summarized in Table III above.

TABLE III. Overview of nodal-line semimetals. The first column specifies the lattice, the second column provides the number of nodal lines (NLs). The third column specifies the mutual nodal line geometry, see also Fig. 1. The last column lists the combination of symmetries that stabilize the nodal line(s), including time-reversal T , inversion P , and sublattice S symmetries.

Lattice	# NL	NL geometry	Symmetry
(10,3)b	1		PT
(10,3)c	1, 3	separate lines	S
(10,3)d	3	chain geometry	PT
(8,3)c	1		PT
(8,3)n	3, 5	pairwise crossings	PT

In addition, for some lattices further symmetries are at play. For lattice (10,3)d there is an additional glide symmetry, which pins one of the nodal lines (marked in red in Fig. 1) to the $k_z = 0$ plane. For lattice (8,3)n, which exhibits three crossing nodal lines (see Fig. 1), a mirror symmetry protects four of the six crossing points, while a fourfold rotation symmetry around the z axis protects the remaining two crossing points. For the details of this mechanism, we refer the interested reader to the discussion in Appendix D.

B. Longer-range interactions and particle-hole symmetry

As discussed above, sublattice symmetry is a crucial symmetry for the nodal-line semimetals occurring in our three-dimensional honeycomb systems. If a system has both sublattice and time-reversal symmetry, their product, denoted by PS , keeps the momentum invariant [40] and defines an effective particle-hole symmetry. This in turn ensures that the nodal lines are located precisely at the Fermi energy (at half filling).

However, sublattice symmetry is a rather fragile symmetry for the electronic systems considered here. Longer-range interactions (such as a next-nearest neighbor hopping), which are not symmetry-forbidden interactions and as such will be present in every realistic system, break sublattice symmetry and thereby immediately destroy particle-hole symmetry as well. For those lattice where the nodal lines are protected by PT symmetry, the nodal lines will shift away from the Fermi energy as a consequence. The result is a toroidal Fermi surface centered around the original nodal lines. This is illustrated for lattice (10,3)b in Fig. 4 below. One can compensate for this shift of the nodal line by introducing a chemical potential and thereby recover the nodal line close to the Fermi energy. (Note, however, that the Fermi line also generically tilts in energy upon breaking sublattice symmetry.) For lattice (10,3)c where the nodal line is protected by sublattice symmetry the inclusion of longer-range interactions, e.g., a next-nearest-neighbor hopping, has a seemingly similar effect in that the resulting Fermi surface also exhibits a toroidal geometry. However, when introducing a chemical potential to compensate for this effect one finds, as illustrated in Fig. 4, that the nodal line no longer exists anywhere in the energy spectrum, but has gapped out up to twelve symmetry-related Dirac points.

C. Drumhead surface states

The topological nature of a nodal-line semimetal manifests itself most directly in the occurrence of so-called drumhead surface states [6–8]. For the sake of completeness, let us briefly recapitulate the elementary steps to see this in the context of the 3D honeycomb systems considered here.

Since all five lattices for which we find nodal lines exhibit sublattice symmetry, their Hamiltonian can be written in the off-diagonal form

$$\mathcal{H}(\vec{k}) = \begin{pmatrix} 0 & A^\dagger(\vec{k}) \\ A(\vec{k}) & 0 \end{pmatrix},$$

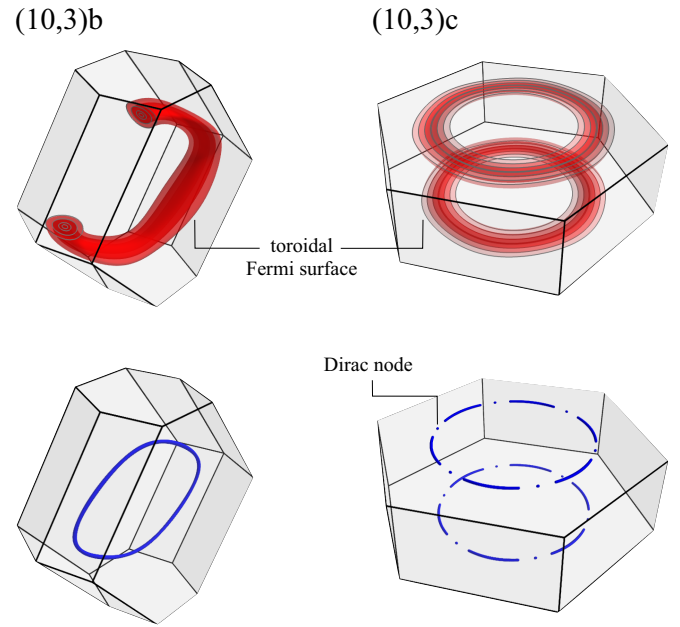


FIG. 4. Toroidal Fermi surfaces for lattices (10,3)b and (10,3)c upon inclusion of a (real) next-nearest-neighbor hopping (top row). In the bottom row we introduce an additional chemical potential that shifts the Fermi energy such that the effect of the next-nearest-neighbor hopping is compensated. While for lattice (10,3)b the nodal line can be recovered this way (see also the discussion in the main text), a more complex situation arises for lattice (10,3)c where we find six isolated Dirac nodes interlaced with small Fermi surface pockets (encompassing another set of six Dirac points).

that is well known in the context of chiral symmetry classes [41]. For such off-diagonal Hamiltonians one can define a winding number

$$W_C = \frac{1}{2\pi} \oint_C d\vec{k} \operatorname{Im}(\operatorname{tr}(A^{-1} \vec{\nabla} A)) \quad (1)$$

for any closed path C in momentum space. In particular, one can consider straight lines through the first Brillouin zone that either pierce through the interior of the nodal line or pass by them on the exterior. For any given nodal line, one of them must carry a nontrivial winding number.

If one now considers the projection of the nodal line to the surface Brillouin zone of a system in a slab geometry, one will find a band of flat surface states (taking the shape of a drumhead) for those momenta for which the corresponding winding number (modulo 2) is nonzero. Examples for both scenarios are shown in Fig. 5.

D. Landau level quantization and bulk flat bands

The nodal line band structure can give rise to another topological phenomenon—the formation of nearly dispersionless bands upon applying an external magnetic field parallel to the plane of the nodal line [10]. These bulk flat bands exhibit a Landau level quantization with an energy spacing that grows like \sqrt{n} with the level index n . This square-root scaling traces back to the linear Dirac dispersion perpendicular to the nodal line and is familiar from the physics of graphene [42]. In the following, we briefly showcase how these generic features

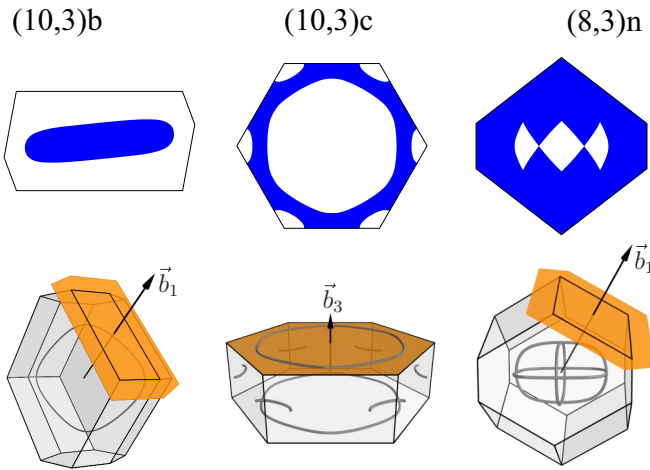


FIG. 5. Drumhead surface states for the nodal-line semimetals of lattices (10,3)b, (10,3)c, and (8,3)n. The bottom row shows the surface Brillouin zones along the projection used above.

of nodal-line semimetals manifest themselves in our three-dimensional honeycomb systems. Working directly with the microscopic model system (in lieu of a continuum approximation [10]) we will focus our discussion on the (10,3)b hyperhoneycomb lattice.

We consider a magnetic field [43] applied in the plane of the nodal line, e.g., along the \hat{x} direction with the nodal line lying in the (k_x, k_y) plane [44]. Upon applying the magnetic field almost dispersionless flat bands evolve in the middle of the spectrum and widen with increasing field strength, as can be seen in the upper panel of Fig. 6, which shows the bulk energy dispersion along the k_z direction perpendicular to the nodal plane. In fact, the nodal line tilts upon applying a magnetic field away from the k_x - k_y plane and acquires a finite

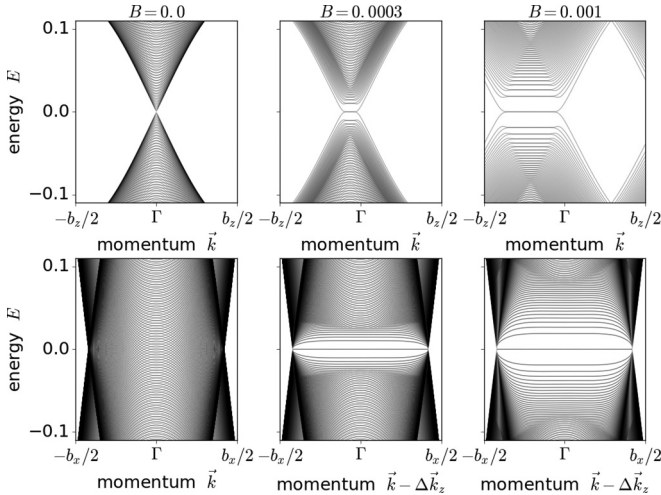


FIG. 6. Formation of Landau levels in the bulk energy spectrum for (10,3)b for a magnetic field applied in plane of the nodal line. The different panels show varying magnetic field strength B . The top row shows the dispersion along the k_z direction perpendicular to the nodal plane. The bottom row shows the dispersion along the k_x direction. The field dependent offset Δk_z chosen such that the latter dispersion traverses the nodal line.

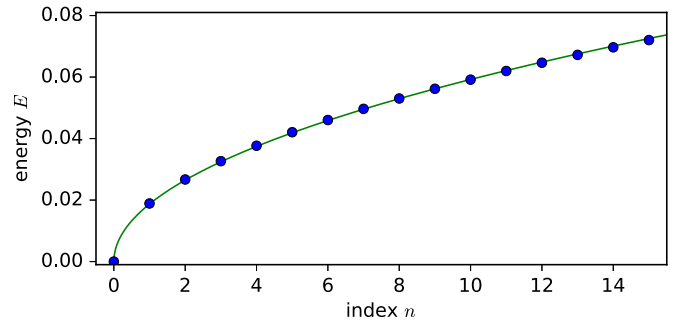


FIG. 7. Spacing of Landau levels in the energy spectrum for the (10,3)b hyperhoneycomb lattice. Green line is a square root fit to the first 14 data points.

extent also along the k_z direction. It is precisely within this k_z region that the nearly dispersionless bands develop. These flat bands constitute Landau levels whose separation is plotted in Fig. 7, clearly revealing the \sqrt{n} growth with the Landau level index n expected for a linear Dirac dispersion [45]. The lower panel in Fig. 6 shows the dispersion along the k_x direction revealing the flat bands precisely in the k_x region inside the nodal line.

Each Landau level is fourfold degenerate, up to a very small Zeeman splitting of the order of 10^{-4} for the magnetic field strengths considered here. This fourfold degeneracy can be explained by realizing that the system effectively sees, for any momentum within the nodal line, two twofold degenerate Dirac nodes (one from each side of the nodal line), similar to the physics of a graphene bilayer as nicely shown in Ref. [10].

Finally, let us note that the Landau levels are not to be confused with the flat surface bands discussed earlier. In fact, the Landau levels discussed here are pure *bulk* features. This can be verified by plotting the spatial localization of their wave function as illustrated in Fig. 8, where the squared amplitude of the wave function (evaluated for a momentum in the middle of the Landau level) is plotted against the y position for a slab geometry. As can be seen, the wave function of the lowest Landau level ($n = 0$) is clearly localized in the middle of the slab. Going to higher Landau levels, one observes a spreading towards the edges of the slab with significant weight remaining in the bulk.

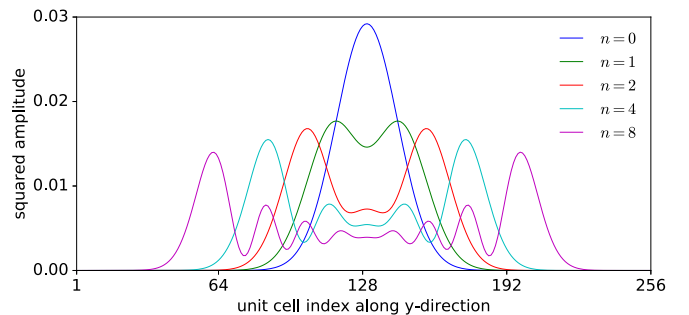


FIG. 8. Squared amplitude of the wave function for the Landau levels for a slab geometry of the (10,3)b hyperhoneycomb lattice with open boundaries along the y direction.

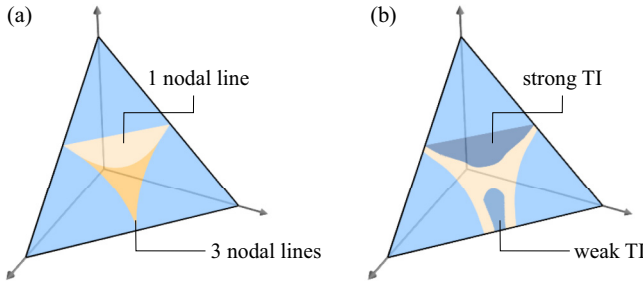


FIG. 9. Schematic phase diagram for (a) the pure tight-binding model and (b) in the presence of spin-orbit coupling ($\lambda = 0.1$). Generically, we find that around the isotropic coupling point ($t_x = t_y = t_z$) there is an extended semimetallic phase (indicated by the orange shading), whereas in the regimes where one of the three coupling strengths dominates one finds gapped, band insulators (indicated by the light blue shading). The actual data shown here is for lattice (10,3)c, which in the absence of spin-orbit coupling exhibits two distinct semimetallic phases with one or three nodal lines, respectively. In the presence of spin-orbit coupling two topological insulator phases emerge that can be classified as strong/weak topological insulators as indicated.

E. Spin-orbit coupling and topological insulators

Probably the most dramatic effect destabilizing the nodal-line band structures in the three-dimensional honeycomb systems at hand is the inclusion of spin-orbit coupling. We find that in the presence of spin-orbit coupling (implemented via a complex next-nearest-neighbor hopping analogous to the work of Kane and Mele [11], see also Appendix C), all nodal-line semimetals generically gap out into topological insulators (TIs). This is illustrated in the exemplary phase diagram for

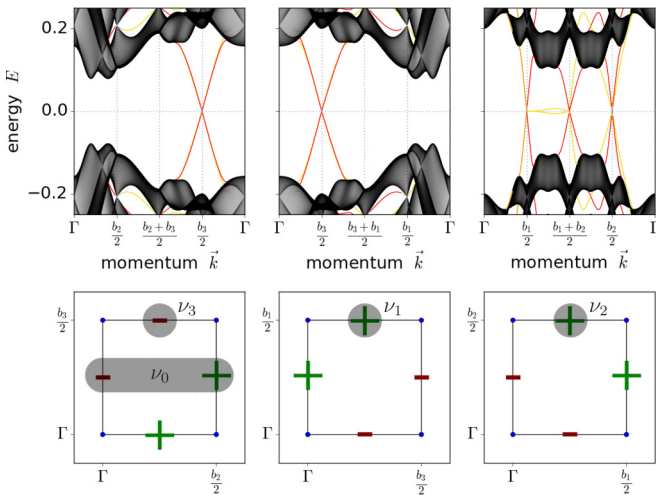


FIG. 10. Strong topological insulator for (10,3)c in the presence of spin-orbit coupling ($\lambda = 0.1$) with topological indices 1;(001). The top row shows the surface energy spectrum along the high-symmetry path connecting the time-reversal invariant momenta (TRIMs). The colored bands indicate surface bands crossing the Fermi energy (with the yellow/red band corresponding to a band on the top/bottom surface). The bottom row shows the change of the time-reversal polarization for different paths between TRIMs (indicated by the blue dots at the corner of the squares).

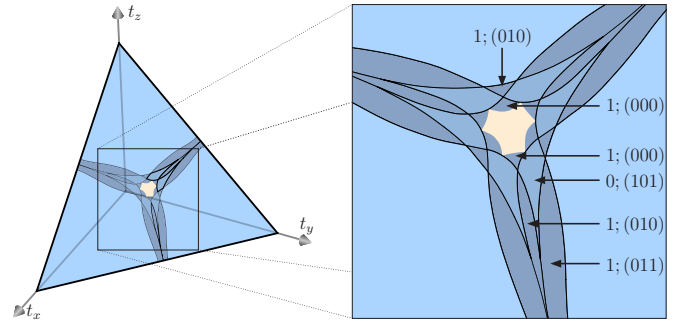


FIG. 11. Kaleidoscope of topological phases for lattice (8,3)c in the presence of spin-orbit coupling ($\lambda = 0.03$).

lattice (10,3)c, which is shown in Fig. 9. Interestingly, for all systems considered here the arising topological insulator is in fact a *strong* topological insulator [which for some systems is flanked by a second parameter regime of a weak topological insulator as is the case for the phase diagram of lattice (10,3)c in Fig. 9]. A precise characterization of the TIs via their topological indices [14] is given in the overview Table I. For the example system (10,3)c the calculation of the topological indices via the surface energy spectrum is illustrated in Fig. 10, with further details provided in Appendix B.

While most nodal-line systems exhibit a relatively simple phase diagram in the presence of spin-orbit coupling, similar to the one shown for lattice (10,3)c in Fig. 9, there is one exception, lattice (8,3)c, where the inclusion of spin-orbit coupling leads to a kaleidoscope of different topological phases as illustrated in Fig. 11. Each line separating two TI phases in Fig. 11 corresponds to a closing of a gap at a *single* time-reversal invariant momentum (TRIM). Since this can change only one cone on the surface, the number of cones switches from even to odd or vice versa, so that every line separates a weak from a strong TI.

Lattices (8,3)c and (8,3)n exhibit another feature occurring in the presence of spin-orbit coupling (besides the formation of a strong TI)—the emergence of Dirac nodes in the spectrum for some parameter regime. For lattice (8,3)n, which exhibits three crossing nodal lines in the absence of spin-orbit coupling, the Dirac nodes emerge precisely at the crossing points (while the remaining nodal lines gap out). The bulk energy

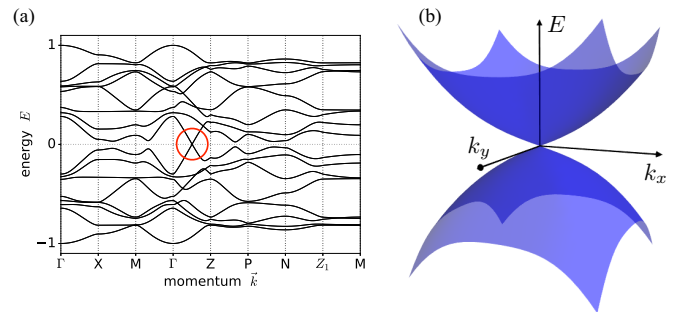


FIG. 12. Spectral features for (8,3)n in the presence of spin-orbit coupling ($\lambda = 0.03$). (a) Bulk energy spectrum along a high-symmetry path with Dirac node highlighted by the red circle. (b) 3D energy spectrum around the Dirac node.

spectrum of lattice (8,3)n is illustrated, along a high-symmetry path, in Fig. 12.

IV. TOPOLOGICAL METALS

For the family of three-dimensional honeycomb models at the heart of this paper there are—besides the ones that give rise to nodal-line semimetals—a number of instances that form metals exhibiting ordinary two-dimensional Fermi surfaces, see the overview of Table I. However, even in this seemingly conventional scenario, it turns out that topology is again at play and the metals are best characterized as *Weyl metals* or *Dirac metals* with a distinct topological feature (such as Weyl or Dirac cones) encompassed by the Fermi surfaces. As such the Fermi surfaces are characterized by a topologically invariant (such as a Chern number), which again leads to the formation of distinct surface features such as Fermi arcs. We will concentrate our discussion on these topological features in the following, after providing some elementary symmetry considerations that motivate the formation of Fermi surfaces in the first place.

A. Symmetry considerations

For the 3D honeycomb systems at hand, we find a metallic behavior for the lattices (10,3)a, (9,3)a, (8,3)a, and (8,3)b as summarized in Table I. The formation of a metal in all these lattices is closely connected to the way sublattice symmetry and inversion are implemented in these lattices.

For the sublattice symmetry there are three cases to distinguish: (i) it might be entirely absent, as is the case for the nonbipartite lattice (9,3)a, (ii) it is implemented with an additional translation in momentum space (see Sec. III A), such as for the lattices (10,3)a, (8,3)a, and (8,3)b of interest here, or (iii) its presence does not require an additional translation in momentum space. The last case is precisely the scenario needed for the formation of nodal lines as discussed in the previous section, while the first two cases naturally lead to the formation of Fermi surfaces as discussed in the following.

Considering inversion symmetry, there are only two possible cases for the lattices at hand—a lattice either breaks inversion symmetry and is chiral or not, see the overview of lattice properties in Table II. If the underlying lattice is inversion symmetric, as is the case for lattices (9,3)a and (8,3)b, then the combination of time-reversal and inversion symmetry, PT , leaves the Hamiltonian invariant and we would naively expect that the system should show nodal line physics. Indeed,

looking at the band structure, one finds that for both lattices the two bands in the middle of the energy spectrum touch along a closed line, which is protected by PT . However, due to the absence (or nontrivial implementation) of sublattice symmetry, the system is not particle-hole symmetric. Consequently, the nodal line(s) do not lie at constant energy (but are tilted) and are not pinned to the Fermi energy. As such the systems generically exhibit Fermi surfaces surrounding the nodal line(s). For the two chiral lattices at hand, lattices (10,3)a and (8,3)a, there is no symmetry protecting nodal lines in the first place, and one would expect these systems to form conventional Fermi surfaces.

B. Hidden Weyl/Dirac nodes

Weyl and Dirac semimetals have recently attracted much attention due to their unique combination of bulk and surface properties [5]. It was already noted early on [1] that band touchings at isolated points in the three-dimensional Brillouin zone can occur frequently and are in fact stable objects. The origin of this stability was later traced back to a topological invariant, the Chern number, that associates an integer charge with each one of them [4]. Charge conservation immediately implies that these so-called Weyl nodes cannot be removed individually, but only in pairs with opposite charge [46,47]. In order for the system to show semimetallic behavior, one needs additional symmetries that pin the energy of at least one pair of Weyl nodes to the Fermi energy. However, even in the absence of such symmetries, the system can show interesting features, particularly when the Weyl nodes are ‘hidden’ within Fermi surfaces and thereby lend their topological properties to the metallic state. Such systems are referred to as Weyl metals. Similarly, a Dirac node—the composition of two Weyl nodes—can be encompassed by a Fermi surface giving rise to what can analogously be referred to as Dirac metal (as opposed to the commonly discussed Dirac *semimetals*). It turns out that these latter scenarios are at play for some of the 3D honeycomb systems considered here.

Specifically, this is the case for lattices (10,3)a and (8,3)a whose spectral features (for the spinless case) are summarized in Figs. 13 and 14, respectively. Both lattices exhibit a single pair of Weyl nodes with one Weyl node located above/below the Fermi energy (as required by sublattice symmetry). The case of lattice (10,3)a is particularly interesting as the Weyl node is located at the intersection of *three* crossing bands, two forming the actual Weyl cone and the third forming a flat band, see Figs. 13(b) and 13(c). This scenario can only

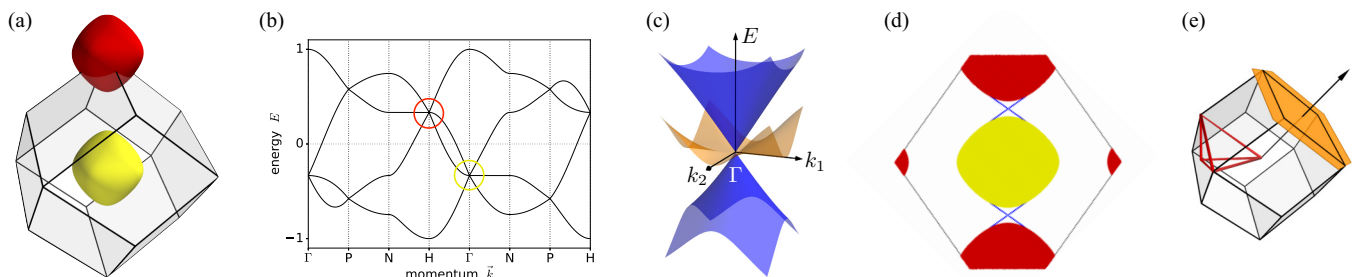


FIG. 13. Overview of the spectral features for the (10,3)a hyperoctagon lattice. (a) Fermi surfaces around the Γ and H points in the Brillouin zone. (b) Bulk energy spectrum along the high-symmetry path indicated in (e). (c) Spin-1 Weyl point (below the Fermi surface) at the Γ point. (d) Surface spectrum with Fermi arcs for the surface Brillouin zone indicated in (e).

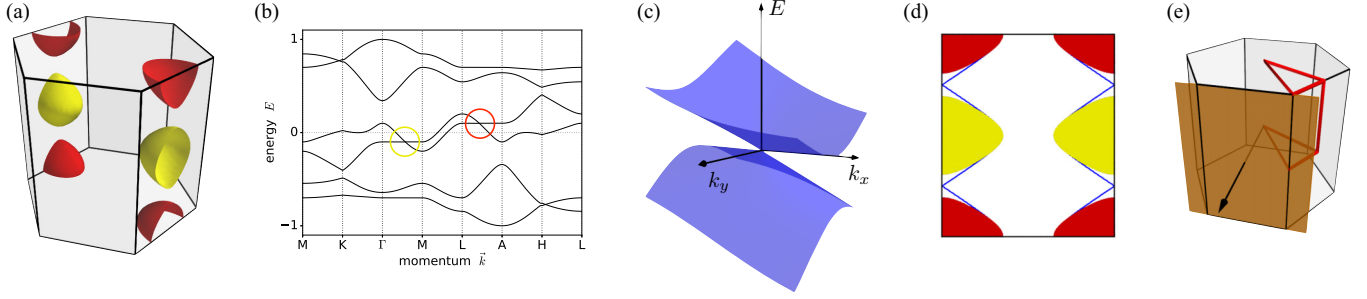


FIG. 14. Overview of the spectral features for lattice (8,3)a. (a) Fermi surfaces around the M and L points in the Brillouin zone. (b) Bulk energy spectrum along the high-symmetry path indicated in (e). (c) Weyl point (below the Fermi surface) close to the M point. (d) Surface spectrum with Fermi arcs for the surface Brillouin zone indicated in (e).

play out at certain high-symmetry points in the Brillouin zone [48] and is referred to as spin-1 Weyl node [27,48–52]. An additional consequence of this spin-1 scenario comes in the form of a higher integer Chern number of ± 2 associated with these Weyl nodes in the bulk and a *pair* of Fermi arcs on the surface, indicated by the blue lines in Fig. 13(d).

For lattice (8,3)a a more conventional scenario is found. The two Fermi surfaces around the M and L points each encompass two Weyl nodes [of which only one is shown along the high-symmetry path in Fig. 14(b)]. As such the Fermi surfaces again carry a total Chern number of ± 2 and the surface energy spectrum shows two Fermi arcs, as shown in Fig. 14(d).

Finally, we briefly mention the two remaining lattices (9,3)a and (8,3)b, which both exhibit Fermi surfaces that enclose nodal lines (instead of Weyl nodes). But as such these Fermi surfaces are *not* endowed with any topological features (since the nodal lines in our models do not exhibit a nontrivial spherical Chern number [20]).

C. Spin-orbit coupling

In the absence of spin-orbit coupling all spectral features discussed above are spin degenerate. The inclusion of spin-orbit coupling will immediately lift this spin degeneracy and the spin-degenerate Dirac cones will split into pairs of Weyl nodes.

A slightly more subtle mechanism is at play for the hyperoctagon lattice (10,3)a where part of the degeneracy remains even in the presence of spin-orbit coupling (SOC). Nonsymmorphic lattice symmetries, in particular a twofold screw symmetry, pin the gapless modes to the high-symmetry points Γ and H , so that the only allowed splitting is in energy. We find that SOC splits the original sixfold degenerate band touching, to a twofold (with charge ± 1) and a fourfold (with charge ± 3) touching, as shown in Figs. 15(b) and 15(c). This degeneracy could be split further by also considering a breaking of the nonsymmorphic lattice symmetries. Figure 15(d) shows the effect of breaking the twofold screw symmetry (in the absence of SOC), which is found to break the charge 4 Dirac node into two charge 2 Dirac nodes. The remaining spin degeneracy can then be destroyed by introducing SOC.

With increasing spin-orbit coupling the Dirac nodes encompassed by the Fermi surfaces move within the Brillouin zone. This reorganization of topological charges becomes most apparent in the surface spectrum, illustrated in Fig. 16. As can be seen in the evolution of these spectra, the Chern numbers associated with the individual Fermi surfaces change sign and the associated Fermi arcs flip their orientation.

V. SUMMARY

Probably the most revealing result of our approach to systematically classify the band structures of three-dimensional

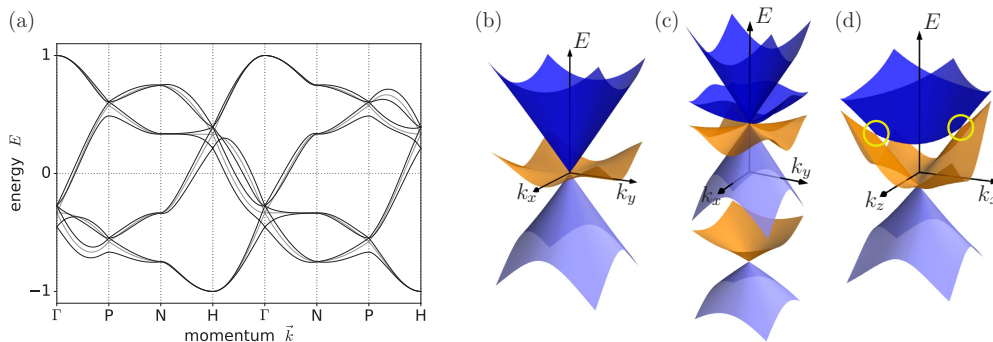


FIG. 15. Effect of spin-orbit coupling on the spin-1 Weyl node of the hyperoctagon lattice (10,3)a. (a) Band structure in the absence/presence of spin-orbit coupling (gray/black lines). (b) The sixfold degeneracy of the spin-1 Weyl node at the Γ point is lifted in the presence of spin-orbit coupling to a twofold and a fourfold band touching as shown in (c). (d) Breaking the twofold screw symmetry (in the absence of spin-orbit coupling), splits the original (charge 4) Weyl node into two (charge 2) Weyl nodes (marked by the yellow circles), which remain spin degenerate.

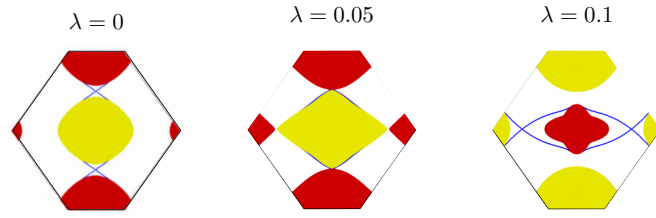


FIG. 16. Evolution of surface states for the (10,3)a hyperoctagon lattice for varying strength of the spin-orbit coupling λ . All spectra exhibit puddles, which originate from the projection of the Fermi surface onto the surface Brillouin zone. They are color coded to reflect the Chern number associated with the Weyl nodes encompassed by the respective Fermi surface. In addition, the surface spectrum exhibits a pair of Fermi arcs (colored in blue) that reflect the connection of the hidden Weyl nodes. With increasing spin-orbit coupling the Weyl nodes reorganize underneath the Fermi surface and the Chern numbers associated with the Fermi surfaces change.

honeycomb systems is the formation of topological features in almost all instances, as summarized in Table I. Amongst these topological band structures, an expansive family of Dirac nodal-line semimetals stands out. Depending on the underlying lattice geometry, these systems exhibit nodal lines forming a variety of mutual geometries, as summarized in Fig. 1. They share many well understood common features such as the protection by PT symmetry (with one exception), the formation of drumhead surface states, and a \sqrt{n} Landau level quantization of bulk flat bands in the presence of an applied magnetic field. Other common features whose origin is less clear include the formation of an *odd* number of nodal lines for all lattice geometries and what appears to be the generic formation of a *strong* topological insulator in the presence of spin-orbit coupling. Besides the formation of nodal-line semimetals we have discussed two instances of Weyl metals, topological metals in which (multiple) Weyl nodes are enclosed by the Fermi surface enriching these systems with a nontrivial bulk Chern number and Fermi arc surface states.

The current investigation of electronic band structures complements our recent work on classifying the band structures of real Majorana fermions relevant to the physics of gapless spin liquids in three-dimensional Kitaev models [28] defined for the same set of elementary tricoordinated lattices. Interestingly, there are a number of instances where the band structures of real and complex fermions differ substantially, see the comparison in Table I. For certain lattice geometries, the Majorana fermions form Weyl semimetals [53] in lieu of conventional (Fermi surface) metals in the corresponding electronic system. The deeper reason for this discrepancy is found in the way projective symmetries and in particular time-reversal symmetry act on the Majorana fermions in contrast to ordinary complex fermions as discussed in detail in Ref. [28].

Beyond electronic and Majorana band structures, the emergence of nodal lines have long been discussed in the context of superconductors [54] and more recently also in magnetic systems with nontrivial magnon bands [55]. Likely, the 3D honeycomb lattices studied in the present work will also reveal nontrivial band structure phenomena for these alternate

systems, but we will leave it to future studies to explore this.

In the realm of materials synthesis, we hope that our work provides inspiration to explore candidate materials that could realize one of the 3D honeycomb systems discussed here. Some of these structures have already been synthesized in 5d Mott insulators, such as the (10,3)b hyperhoneycomb lattice in the iridate Li_2IrO_3 [33,34], and investigated for their unusual magnetism. In the context of these Kitaev materials [56], other possible routes to synthesize 3D honeycomb systems have been proposed, including the use of metal-organic frameworks [35]. To explore the semimetals discussed in the current paper, the most natural starting point probably is to turn to three-dimensional graphene/carbon networks, some of which are already known to exhibit nodal-line semimetals [30]. The relatively simple structures discussed here (with only a few sites in their unit cell compared to several tens or hundreds for some of the more complex networks) are hopefully within experimental reach, like the recent realization of a (10,3)a K_4 carbon structure [31,32].

ACKNOWLEDGMENTS

We acknowledge insightful discussions with S. Parameswaran, K. O'Brien, M. G. Yamada, and V. Dwivedi. This work was partially supported by the DFG within the CRC 1238 (project C02). The numerical simulations were performed on the CHEOPS cluster at RRZK Cologne.

APPENDIX A: TRICOORDINATED LATTICE GEOMETRIES

To make the paper at hand fully self-contained, we provide in the following the details of all the tricoordinated lattices discussed in the main text. In particular, we provide the lattice vectors and their corresponding reciprocal lattice vectors, as well as the positions of the lattice sites within the unit cell. Details on the symmetry group for all lattices can be found in Table II.

1. (10,3)a

The lattice vectors of the chiral hyperoctagon or (10,3)a lattice are given by

$$\begin{aligned} \mathbf{a}_1 &= (1, 0, 0), & \mathbf{a}_2 &= \left(\frac{1}{2}, \frac{1}{2}, -\frac{1}{2}\right), \\ \mathbf{a}_3 &= \left(\frac{1}{2}, \frac{1}{2}, \frac{1}{2}\right) \end{aligned}$$

and their corresponding reciprocal lattice vectors are

$$\begin{aligned} \mathbf{b}_1 &= 2\pi(1, -1, 0), & \mathbf{b}_2 &= 2\pi(0, 1, -1), \\ \mathbf{b}_3 &= 2\pi(0, 1, 1). \end{aligned}$$

This lattice has four sites per unit cell that are located at

$$\begin{aligned} \mathbf{r}_1 &= \frac{1}{8}(1, 1, 1), & \mathbf{r}_2 &= \frac{1}{8}(5, 3, -1) \\ \mathbf{r}_3 &= \frac{1}{8}(3, 1, -1), & \mathbf{r}_4 &= \frac{1}{8}(7, 3, 1). \end{aligned}$$

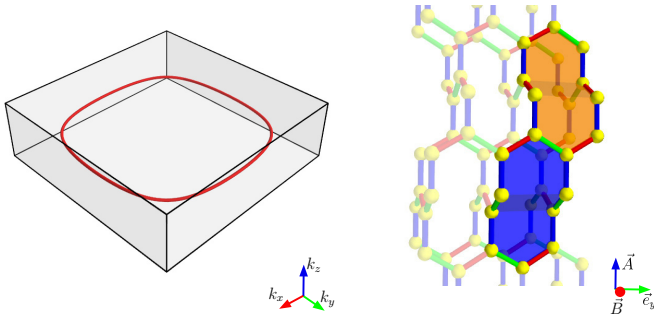


FIG. 17. Left: Visualization of the nodal line of the deformed hyperhoneycomb lattice in the rectangular Brillouin zone. Right: The deformed hyperhoneycomb lattice with enlarged unit cell and orthogonal lattice vectors. Of the eight plaquettes per unit cell, only two enclose a magnetic flux (for $\mathbf{B} = B_0 \hat{e}_x$), which we marked in orange and blue.

2. (10,3)b

The (10,3)b or hyperhoneycomb lattice has, in its original realization, the translation vectors

$$\mathbf{a}_1 = (-1, 1, -2), \quad \mathbf{a}_2 = (-1, 1, 2), \\ \mathbf{a}_3 = (2, 4, 0).$$

Their corresponding reciprocal lattice vectors are given by

$$\mathbf{b}_1 = 2\pi \left(-\frac{1}{3}, \frac{1}{6}, -\frac{1}{4} \right), \quad \mathbf{b}_2 = 2\pi \left(-\frac{1}{3}, \frac{1}{6}, \frac{1}{4} \right), \\ \mathbf{b}_3 = 2\pi \left(\frac{1}{6}, \frac{1}{6}, 0 \right).$$

This lattice has also four sites per unit cell that are located at

$$\mathbf{r}_1 = (0, 0, 0), \quad \mathbf{r}_2 = (1, 2, 1) \\ \mathbf{r}_3 = (1, 1, 0), \quad \mathbf{r}_4 = (2, 3, 1).$$

In order to include a magnetic field and still retain two good quantum numbers in reciprocal space, it is convenient to deform the hyperhoneycomb lattice. First we use that the angle between the two different zigzag chains in \mathbf{a}_1 and \mathbf{a}_2 direction can be chosen arbitrarily. Thus to simplify the calculation we set them to be orthogonal, as, e.g., done in Ref. [26]. By doubling the unit cell in the z direction, we can furthermore set \mathbf{a}_3 to be orthogonal to the first two lattice vectors, \mathbf{a}_1 and \mathbf{a}_2 . The price we pay is that there are now eight sites per unit cell. Solving the tight-binding model on the (deformed) hyperhoneycomb lattice, we find that the BZ is now rectangular and the nodal line is located in the $k_z = 0$ plane, as shown on the left of Fig. 17. This deformation also ensures that upon applying a magnetic field in the x direction—i.e., $\mathbf{B} = B_0 \hat{e}_x$ with vector potential given by $\mathbf{A} = B_0 y \hat{e}_z$ —only two of the eight plaquettes per unit cell enclose a magnetic flux. These are shown on the right side of Fig. 17, marked in orange and blue. For more details on the plaquettes per unit cell for the hyperhoneycomb lattice, we refer the reader to the discussion in Ref. [28]. For the deformed lattice, the lattice vectors become

$$\mathbf{a}_1 = (\sqrt{3}, 0, 0), \quad \mathbf{a}_2 = (0, \sqrt{3}, 0), \\ \mathbf{a}_3 = (0, 0, 6),$$

and the reciprocal lattice vectors

$$\mathbf{b}_1 = 2\pi \left(\frac{1}{\sqrt{3}}, 0, 0 \right), \quad \mathbf{b}_2 = 2\pi \left(0, \frac{1}{\sqrt{3}}, 0 \right), \\ \mathbf{b}_3 = 2\pi \left(0, 0, \frac{1}{6} \right).$$

The eight sites within the unit cell are localized at

$$\mathbf{r}_1 = \left(-\frac{\sqrt{3}}{4}, -\frac{\sqrt{3}}{4}, -\frac{11}{4} \right), \quad \mathbf{r}_2 = \left(-\frac{\sqrt{3}}{4}, -\frac{\sqrt{3}}{4}, -\frac{7}{4} \right) \\ \mathbf{r}_3 = \left(\frac{\sqrt{3}}{4}, -\frac{\sqrt{3}}{4}, -\frac{5}{4} \right), \quad \mathbf{r}_4 = \left(\frac{\sqrt{3}}{4}, -\frac{\sqrt{3}}{4}, -\frac{1}{4} \right) \\ \mathbf{r}_5 = \left(\frac{\sqrt{3}}{4}, \frac{\sqrt{3}}{4}, \frac{1}{4} \right), \quad \mathbf{r}_6 = \left(\frac{\sqrt{3}}{4}, \frac{\sqrt{3}}{4}, \frac{5}{4} \right) \\ \mathbf{r}_7 = \left(-\frac{\sqrt{3}}{4}, \frac{\sqrt{3}}{4}, \frac{7}{4} \right), \quad \mathbf{r}_8 = \left(-\frac{\sqrt{3}}{4}, \frac{\sqrt{3}}{4}, \frac{11}{4} \right).$$

3. (10,3)c

The (10,3)c lattice is closely related to the hyperhoneycomb lattice, except that its zigzag chains run along three different directions that are 120° rotated against each other (see Fig. 2). Its lattice vectors are given by

$$\mathbf{a}_1 = (1, 0, 0), \quad \mathbf{a}_2 = \left(-\frac{1}{2}, \frac{\sqrt{3}}{2}, 0 \right), \\ \mathbf{a}_3 = \left(0, 0, \frac{3\sqrt{3}}{21} \right),$$

and the corresponding reciprocal lattice vectors are

$$\mathbf{b}_1 = 2\pi \left(1, \frac{1}{\sqrt{3}}, 0 \right), \quad \mathbf{b}_2 = 2\pi \left(0, \frac{2}{\sqrt{3}}, 0 \right), \\ \mathbf{b}_3 = 2\pi \left(0, 0, \frac{2}{3\sqrt{3}} \right).$$

This lattice has six sites per unit cell, which are located at

$$\mathbf{r}_1 = \frac{1}{4\sqrt{3}}(\sqrt{3}, 1, 2), \quad \mathbf{r}_2 = \frac{1}{4\sqrt{3}}(3\sqrt{3}, 1, 8) \\ \mathbf{r}_3 = \frac{1}{4\sqrt{3}}(2\sqrt{3}, 4, 14), \quad \mathbf{r}_4 = \frac{1}{4\sqrt{3}}(3\sqrt{3}, 1, 4) \\ \mathbf{r}_5 = \frac{1}{4\sqrt{3}}(2\sqrt{3}, 4, 10), \quad \mathbf{r}_6 = \frac{1}{4\sqrt{3}}(\sqrt{3}, 1, 16).$$

4. (10,3)d

The inversion-symmetric (10,3)d lattice is closely related to the chiral hyperoctagon (10,3)a lattice, except that the rotation of the ‘square’ spirals is alternating as shown in Fig. 2. Its lattice vectors can be chosen as

$$\mathbf{a}_1 = (1, -1, 0), \quad \mathbf{a}_2 = (1, 1, 0), \\ \mathbf{a}_3 = (0, 0, 1)$$

with the reciprocal lattice vectors given by

$$\begin{aligned}\mathbf{b}_1 &= \pi(1, -1, 0), & \mathbf{b}_2 &= \pi(1, 1, 0), \\ \mathbf{b}_3 &= \pi(0, 0, 2).\end{aligned}$$

The (10,3)d lattice has eight sites per unit cell that are located at

$$\begin{aligned}\mathbf{r}_1 &= \frac{1}{4}(a, b, 1), & \mathbf{r}_2 &= \frac{1}{4}(0, a + b, 2) \\ \mathbf{r}_3 &= \frac{1}{4}(-a, b, 3), & \mathbf{r}_4 &= \frac{1}{4}(0, -a + b, 4) \\ \mathbf{r}_5 &= \frac{1}{4}(0, a - b, 3), & \mathbf{r}_6 &= \frac{1}{4}(-a, -b, 2) \\ \mathbf{r}_7 &= \frac{1}{4}(0, -a - b, 1), & \mathbf{r}_8 &= \frac{1}{4}(a, -b, 4),\end{aligned}$$

where we used the same conventions,

$$a = 4 - 2\sqrt{2}m \quad b = 2,$$

as in Ref. [29].

5. (9,3)a

The (9,3)a lattice is the only example of the lattices at hand that is not bipartite. In its most symmetric form, its lattice vectors are given by

$$\begin{aligned}\mathbf{a}_1 &= \frac{1}{3}(-\mathbf{a} + \mathbf{b} + \mathbf{c}), & \mathbf{a}_2 &= \frac{1}{3}(-\mathbf{a} - 2\mathbf{b} + \mathbf{c}), \\ \mathbf{a}_3 &= \frac{1}{3}(2\mathbf{a} + \mathbf{b} + \mathbf{c}),\end{aligned}$$

where

$$\mathbf{a} = (1, 0, 0), \quad \mathbf{b} = \left(-\frac{1}{2}, \frac{\sqrt{3}}{2}, 0\right), \quad \mathbf{c} = (0, 0, \alpha)$$

with

$$\alpha = \frac{\sqrt{6(4 + \sqrt{3})}}{1 + 2\sqrt{3}}, \quad \delta_f = \frac{\sqrt{3}}{1 + 2\sqrt{3}}, \quad \delta_h = \frac{29 - 3\sqrt{3}}{132}.$$

The corresponding reciprocal lattice vectors then become

$$\begin{aligned}\mathbf{b}_1 &= 2\pi\left(-1, \frac{1}{\sqrt{3}}, \frac{1}{\alpha}\right), & \mathbf{b}_2 &= 2\pi\left(0, -\frac{2}{\sqrt{3}}, \frac{1}{\alpha}\right), \\ \mathbf{b}_3 &= 2\pi\left(1, \frac{1}{\sqrt{3}}, \frac{1}{\alpha}\right).\end{aligned}$$

It has twelve sites per unit cell which are located at

$$\begin{aligned}\mathbf{r}_1 &= \delta_f \mathbf{a}, & \mathbf{r}_2 &= 2\delta_h \mathbf{a} + \delta_h \mathbf{b} + \frac{1}{12} \mathbf{c} \\ \mathbf{r}_3 &= \delta_h (\mathbf{a} + \mathbf{b}), & \mathbf{r}_4 &= \delta_h \mathbf{a} + 2\delta_h \mathbf{b} - \frac{1}{12} \mathbf{c} \\ \mathbf{r}_5 &= \delta_f \mathbf{b}, & \mathbf{r}_6 &= -\delta_h \mathbf{a} + \delta_h \mathbf{b} + \frac{1}{12} \mathbf{c} \\ \mathbf{r}_7 &= -\delta_f \mathbf{a}, & \mathbf{r}_8 &= -2\delta_h \mathbf{a} - \delta_h \mathbf{b} - \frac{1}{12} \mathbf{c} \\ \mathbf{r}_9 &= -\delta_f (\mathbf{a} + \mathbf{b}), & \mathbf{r}_{10} &= -\delta_h \mathbf{a} - 2\delta_h \mathbf{b} + \frac{1}{12} \mathbf{c} \\ \mathbf{r}_{11} &= -\delta_f \mathbf{b}, & \mathbf{r}_{12} &= \delta_h \mathbf{a} - \delta_h \mathbf{b} - \frac{1}{12} \mathbf{c}.\end{aligned}$$

A simpler but also less symmetric version of the lattice can be found in Ref. [28].

6. (8,3)a

The (8,3)a lattice is a chiral lattice. For all computations shown in this paper, we use the version where all triangular spirals are rotating clockwise [57], as in Ref. [28]. Its lattice vectors are given by

$$\begin{aligned}\mathbf{a}_1 &= (1, 0, 0), & \mathbf{a}_2 &= \left(-\frac{1}{2}, \frac{\sqrt{3}}{2}, 0\right), \\ \mathbf{a}_3 &= \left(0, 0, \frac{3\sqrt{2}}{5}\right)\end{aligned}$$

and its reciprocal lattice vectors by

$$\begin{aligned}\mathbf{b}_1 &= 2\pi\left(1, \frac{1}{\sqrt{3}}, 0\right), & \mathbf{b}_2 &= 2\pi\left(0, \frac{2}{\sqrt{3}}, 0\right), \\ \mathbf{b}_3 &= 2\pi\left(0, 0, \frac{5\sqrt{2}}{6}\right).\end{aligned}$$

The lattice has six sites per unit cell at positions

$$\begin{aligned}\mathbf{r}_1 &= \left(\frac{1}{2}, \frac{\sqrt{3}}{10}, 0\right), & \mathbf{r}_2 &= \left(\frac{3}{5}, \frac{\sqrt{3}}{5}, \frac{2\sqrt{2}}{5}\right) \\ \mathbf{r}_3 &= \left(\frac{1}{10}, \frac{3\sqrt{3}}{10}, \frac{\sqrt{2}}{5}\right), & \mathbf{r}_4 &= \left(\frac{2}{5}, \frac{\sqrt{3}}{5}, \frac{\sqrt{2}}{5}\right) \\ \mathbf{r}_5 &= \left(0, \frac{2\sqrt{3}}{5}, 0\right), & \mathbf{r}_6 &= \left(-\frac{1}{10}, \frac{3\sqrt{3}}{10}, \frac{2\sqrt{2}}{5}\right).\end{aligned}$$

7. (8,3)b

The (8,3)b lattice is closely related to the (8,3)a lattice, except that it is inversion symmetric with alternating rotation directions of the triangular spirals, see Fig. 2. Its lattice translation vectors are given by

$$\begin{aligned}\mathbf{a}_1 &= \left(\frac{1}{2}, \frac{1}{2\sqrt{3}}, \frac{\sqrt{2}}{5\sqrt{3}}\right), & \mathbf{a}_2 &= \left(0, \frac{1}{\sqrt{3}}, \frac{2\sqrt{2}}{5\sqrt{3}}\right), \\ \mathbf{a}_3 &= \left(0, 0, \frac{\sqrt{6}}{5}\right),\end{aligned}$$

and the corresponding reciprocal lattice vectors are

$$\begin{aligned}\mathbf{b}_1 &= 2\pi(2, 0, 0), & \mathbf{b}_2 &= 2\pi(-1, \sqrt{3}, 0), \\ \mathbf{b}_3 &= 2\pi\left(0, -\frac{2}{\sqrt{3}}, \frac{5}{\sqrt{6}}\right).\end{aligned}$$

It also has six sites per unit cell at positions

$$\begin{aligned} \mathbf{r}_1 &= \left(\frac{1}{10}, \frac{1}{2\sqrt{3}}, \frac{\sqrt{2}}{5\sqrt{3}} \right), & \mathbf{r}_2 &= \left(\frac{1}{5}, \frac{\sqrt{3}}{5}, \frac{\sqrt{6}}{5} \right) \\ \mathbf{r}_3 &= \left(\frac{3}{10}, \frac{11}{10\sqrt{3}}, \frac{4\sqrt{2}}{5\sqrt{3}} \right), & \mathbf{r}_4 &= \left(\frac{1}{5}, \frac{2}{5\sqrt{3}}, \frac{2\sqrt{2}}{5\sqrt{3}} \right) \\ \mathbf{r}_5 &= \left(\frac{3}{10}, \frac{3\sqrt{3}}{10}, \frac{\sqrt{6}}{5} \right), & \mathbf{r}_6 &= \left(\frac{2}{5}, \frac{1}{\sqrt{3}}, \sqrt{\frac{2}{3}} \right). \end{aligned}$$

8. (8,3)c

The lattice vectors of the inversion-symmetric (8,3)c lattice are chosen as

$$\begin{aligned} \mathbf{a}_1 &= (1, 0, 0), & \mathbf{a}_2 &= \left(-\frac{1}{2}, \frac{\sqrt{3}}{2}, 0 \right), \\ \mathbf{a}_3 &= \left(0, 0, \frac{2}{5} \right) \end{aligned}$$

and the reciprocal lattice vectors become

$$\begin{aligned} \mathbf{b}_1 &= 2\pi \left(1, \frac{1}{\sqrt{3}}, 0 \right), & \mathbf{b}_2 &= 2\pi \left(0, \frac{2}{\sqrt{3}}, 0 \right), \\ \mathbf{b}_3 &= 2\pi \left(0, 0, \frac{5}{2} \right). \end{aligned}$$

It has eight sites per unit cell that are located at

$$\begin{aligned} \mathbf{r}_1 &= \left(-\frac{1}{5}, \frac{4}{5\sqrt{3}}, \frac{1}{10} \right), & \mathbf{r}_2 &= \left(0, \frac{1}{\sqrt{3}}, \frac{1}{10} \right) \\ \mathbf{r}_3 &= \left(\frac{3}{10}, \frac{7}{10\sqrt{3}}, \frac{3}{10} \right), & \mathbf{r}_4 &= \left(\frac{1}{2}, \frac{1}{10\sqrt{3}}, \frac{3}{10} \right) \\ \mathbf{r}_5 &= \left(0, \frac{7}{5\sqrt{3}}, \frac{1}{10} \right), & \mathbf{r}_6 &= \left(\frac{1}{5}, \frac{4}{5\sqrt{3}}, \frac{1}{10} \right) \\ \mathbf{r}_7 &= \left(\frac{1}{2}, \frac{1}{2\sqrt{3}}, \frac{3}{10} \right), & \mathbf{r}_8 &= \left(\frac{7}{10}, \frac{7}{10\sqrt{3}}, \frac{3}{10} \right). \end{aligned}$$

9. (8,3)n

The (8,3)n lattice is again an inversion-symmetric lattice. Using

$$\begin{aligned} \mathbf{a} &= (1, 0, 0), & \mathbf{b} &= (0, 1, 0), & \mathbf{c} &= (0, 0, \alpha) \\ \alpha &= \frac{4}{2\sqrt{3} + \sqrt{2}}, & x &= \frac{\sqrt{3} + \sqrt{2}}{2(2\sqrt{3} + \sqrt{2})}, & z &= \frac{1}{8}, \end{aligned}$$

we can express the lattice translation vectors as

$$\mathbf{a}_1 = \mathbf{a}, \quad \mathbf{a}_2 = \mathbf{b}, \quad \mathbf{a}_3 = \frac{1}{2}(\mathbf{a} + \mathbf{b} + \mathbf{c})$$

while the corresponding reciprocal lattice vectors become

$$\begin{aligned} \mathbf{b}_1 &= 2\pi \left(1, 0, -\frac{1}{\alpha} \right), & \mathbf{b}_2 &= 2\pi \left(0, 1, -\frac{1}{\alpha} \right), \\ \mathbf{b}_3 &= 2\pi \left(0, 0, \frac{2}{\alpha} \right). \end{aligned}$$

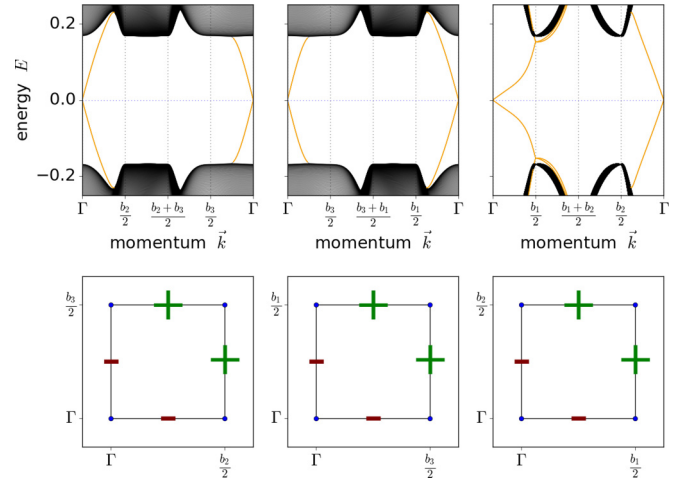


FIG. 18. Surface energy spectra along high-symmetry paths for the strong topological insulator 1; (000) for (10,3)b at the isotropic point $t_x = t_y = t_z = 1/3$ with $\lambda = 0.1$.

This lattice has a rather large unit cell consisting of 16 sites that are located at

$$\begin{aligned} \mathbf{r}_1 &= x\mathbf{a} + \left(\frac{1}{2} - x \right)\mathbf{b} + \frac{1}{4}\mathbf{c} \\ \mathbf{r}_2 &= (1-x)\mathbf{a} + \left(\frac{1}{2} - x \right)\mathbf{b} + \frac{1}{4}\mathbf{c} \\ \mathbf{r}_3 &= \left(\frac{1}{2} + x \right)\mathbf{a} + \frac{1}{2}\mathbf{b} + \left(\frac{1}{2} - z \right)\mathbf{c} \\ \mathbf{r}_4 &= (1-x)\mathbf{a} + \left(\frac{1}{2} + x \right)\mathbf{b} + \frac{1}{4}\mathbf{c} \\ \mathbf{r}_5 &= x\mathbf{a} + \left(\frac{1}{2} + x \right)\mathbf{b} + \frac{1}{4}\mathbf{c} \\ \mathbf{r}_6 &= \left(\frac{1}{2} - x \right)\mathbf{a} + \frac{1}{2}\mathbf{b} + \left(\frac{1}{2} - z \right)\mathbf{c} \\ \mathbf{r}_7 &= (1-x)\mathbf{b} + z\mathbf{c} \\ \mathbf{r}_8 &= x\mathbf{b} + z\mathbf{c} \\ \mathbf{r}_9 &= \left(\frac{1}{2} - x \right)\mathbf{a} + x\mathbf{b} + \frac{1}{4}\mathbf{c} \\ \mathbf{r}_{10} &= \frac{1}{2}\mathbf{a} + \left(\frac{1}{2} - x \right)\mathbf{b} + \left(\frac{1}{2} - z \right)\mathbf{c} \\ \mathbf{r}_{11} &= \left(\frac{1}{2} + x \right)\mathbf{a} + x\mathbf{b} + \frac{1}{4}\mathbf{c} \end{aligned}$$

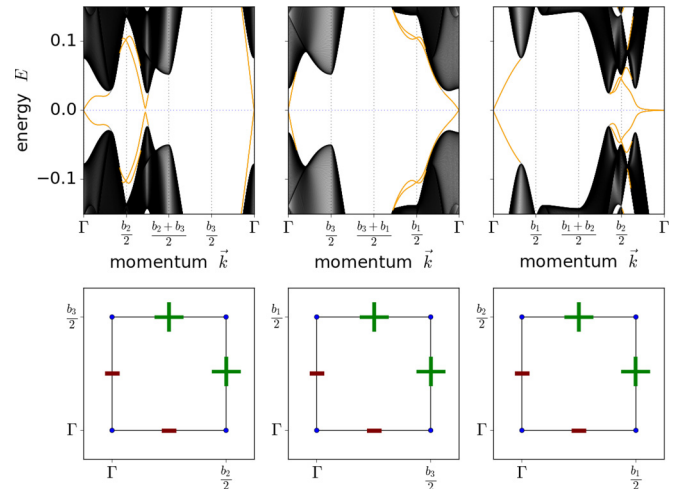


FIG. 19. Surface energy spectra along high-symmetry paths for the strong topological insulator 1; (000) for (10,3)d at the isotropic point with $\lambda = 0.03$.

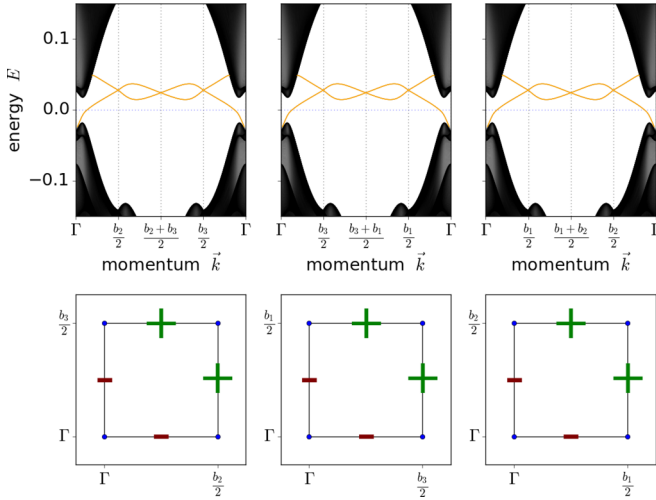


FIG. 20. Surface energy spectra along high-symmetry paths for the strong topological insulator 1;(000) for (9,3)a at $t_z = 0.475$, $t_x = t_y = 0.2625$, and $\lambda = 0.03$.

$$\begin{aligned} \mathbf{r}_{12} &= \left(\frac{1}{2} + x\right)\mathbf{a} + (1 - x)\mathbf{b} + \frac{1}{4}\mathbf{c} \\ \mathbf{r}_{13} &= \frac{1}{2}\mathbf{a} + \left(\frac{1}{2} + x\right)\mathbf{b} + \left(\frac{1}{2} - z\right)\mathbf{c} \\ \mathbf{r}_{14} &= \left(\frac{1}{2} - x\right)\mathbf{a} + (1 - x)\mathbf{b} + \frac{1}{4}\mathbf{c} \\ \mathbf{r}_{15} &= x\mathbf{a} + z\mathbf{c} \\ \mathbf{r}_{16} &= (1 - x)\mathbf{a} + z\mathbf{c}. \end{aligned}$$

It has a fourfold rotation symmetry around the z axis, as well as several mirror symmetries.

APPENDIX B: TOPOLOGICAL INSULATOR CLASSIFICATION

In three spatial dimensions, topological insulators (TIs) can be classified [14] by four \mathbb{Z}_2 topological indices $\nu_0; (\nu_1 \nu_2 \nu_3)$. The first index ν_0 differentiates between strong ($\nu_0 = 1$) and

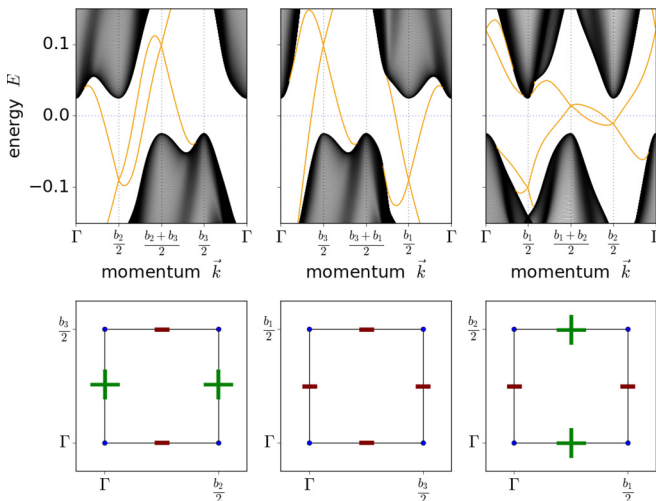


FIG. 21. Surface energy spectra along high-symmetry paths for the weak topological insulator 0;(101) for (8,3)b at $t_z = 0.2$, $t_x = t_y = 0.4$, and $\lambda = 0.1$.

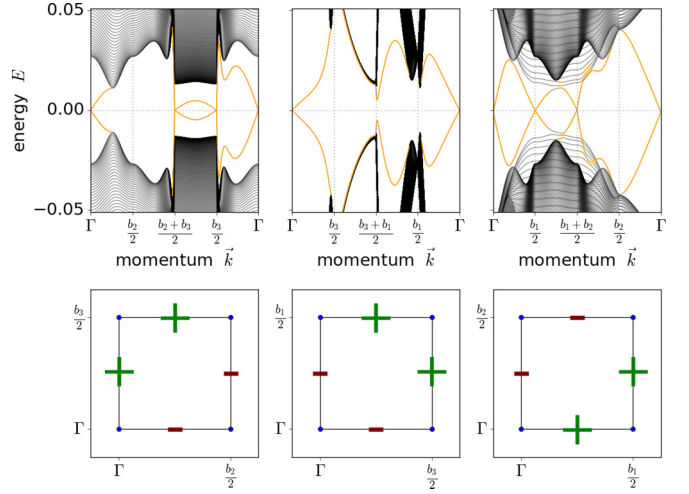


FIG. 22. Surface energy spectra along high-symmetry paths for the strong topological insulator 1;(010) for (8,3)c at $t_z = 0.2$, $t_x = t_y = 0.4$, and $\lambda = 0.03$.

weak ($\nu_0 = 0$) topological insulators. Technically, it states whether the TI exhibits an odd (strong) or even (weak) number of Dirac cones on the surface. As such, a strong TI enjoys a higher level of topological protection, since in contrast to their weak counterparts their surface Dirac cones cannot be gapped out by simply merging pairs of Dirac cones. In more general terms, a strong TI is an intrinsically three-dimensional topological state, while a weak TI can be seen as layered composite of two-dimensional topological states (such as the quantum spin Hall states) [13–15]. The remaining indices $(\nu_1 \nu_2 \nu_3)$ are the so-called weak indices, which further specify the positions of the Dirac cones on the various surfaces of the TI.

Topologically protected Dirac cones on the surface of a three-dimensional TI cannot appear at arbitrary momenta in the surface Brillouin zone but are fixed to certain high-symmetry points [13–15], i.e., the set of time-reversal invariant momenta (TRIMs). These TRIMs can be found at linear combinations of half reciprocal lattice vectors \vec{b}_i , i.e.,

$$\Lambda_{n_1 n_2 n_3} = \frac{1}{2} \sum n_i \vec{b}_i \quad \text{with } n_i \in \{0, 1\}.$$

The relevance of the TRIMs here is that they can be used to calculate the topological indices $\nu_0; (\nu_1 \nu_2 \nu_3)$ mentioned above. Specifically, we have

$$\begin{aligned} (-1)^{\nu_0} &= \prod_{n_1, n_2, n_3=0}^1 \delta_{n_1 n_2 n_3} \\ (-1)^{\nu_i} &= \prod_{\substack{n_j \neq i=0,1 \\ n_i=1}} \delta_{n_1 n_2 n_3}, \end{aligned}$$

where $\delta = \pm 1$ is the time-reversal polarization (TRP) at the TRIM defined by n_1, n_2, n_3 . To determine the indices, it is in fact not necessary to calculate this time-reversal polarization explicitly, but it suffices to determine its change between two TRIMs. Following Ref. [14], the simplest way to do so is to count the number of surface bands crossing the Fermi energy between two TRIMs. If this number is odd, the corresponding TRP changes sign, otherwise not. To determine

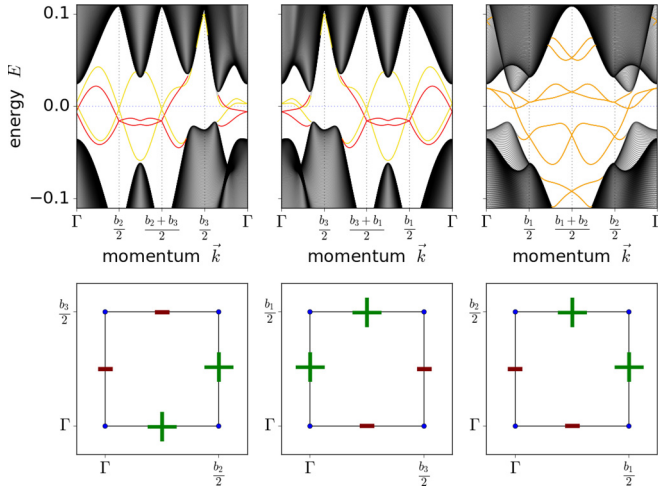


FIG. 23. Surface energy spectra along high-symmetry paths for the strong topological insulator 1;(001) for (8,3)n at $t_z = 0.51$, $t_x = t_y = 0.245$, and $\lambda = 0.1$.

the topological indices, it then suffices to calculate the TRP change for a fixed path between two TRIMs to obtain the weak topological indices and to calculate the product of TRP changes on opposite paths to obtain the strong index.

In the following, we document the determination of topological indices for the topological insulators found in the various 3D honeycomb systems at the heart of the current study. To do so, we provide an illustration of the surface energy spectra, as shown in Figs. 18–23, along a high-symmetry path connecting the TRIMs and indicate the change of the TRP along this path. The surface bands are marked in red or yellow, depending on whether they are located at the upper or lower surface. If the bands are degenerated they are marked in orange.

APPENDIX C: TIGHT-BINDING HAMILTONIAN

In the main text of our paper, we use the tight-binding Hamiltonian

$$H = \sum_{\langle i,j \rangle} t_{ij} (\mathbf{c}_i^\dagger \sigma_0 \mathbf{c}_j + \text{H.c.}) + i \sum_{\langle\langle i,j \rangle\rangle} \sum_l v_{\text{KM}} (\mathbf{c}_i^\dagger (\vec{d}_{il} \times \vec{d}_{lj}) \cdot \vec{\sigma} \mathbf{c}_j + \text{H.c.}) \quad (\text{C1})$$

with

$$\mathbf{c}_i^\dagger = \begin{pmatrix} c_{i,\uparrow}^\dagger \\ c_{i,\downarrow}^\dagger \end{pmatrix}, \quad \vec{\sigma} = \begin{pmatrix} \sigma_x \\ \sigma_y \\ \sigma_z \end{pmatrix}, \quad \text{and} \quad \vec{d}_{ij} = \frac{\vec{r}_{ij}}{|\vec{r}_{ij}|}. \quad (\text{C2})$$

We generically allow the strength of the nearest-neighbor hopping, t_{ij} , to be anisotropic when mapping out the phase diagram. The spin-orbit coupling term is implemented via a complex next-nearest-neighbor hopping, similar to the implementation in Ref. [14].

APPENDIX D: EFFECT OF ADDITIONAL SYMMETRIES ON NODAL LINE SEMIMETALS

1. (10,3)d

The glide symmetry in (10,3)d is implemented in k space by

$$H(k_x, k_y, k_z) = U_G^\dagger H(k_x, k_y, -k_z) U_G, \quad (\text{D1})$$

where U_G is a unitary matrix that depends on \mathbf{k} . Thus, in the $k_z = 0$ plane, the Hamiltonian is invariant under the glide symmetry and all its eigenstates can be labeled by their glide eigenvalues. These turn out to be inverted at the Γ point, compared to the K point located at the edge of the Brillouin zone, very similar to what was found in Ref. [29]. Thus, as long as the glide symmetry remains intact, the nodal line in the $k_z = 0$ cannot be gapped out.

2. (8,3)n

The lattice (8,3)n exhibits several intersecting nodal lines as depicted in Fig. 1. These remain stable even with anisotropic coupling due to the protection by a mirror symmetry, implemented as

$$H(k_x, k_y, k_z) = U_M^\dagger H(k_x, k_y, -k_z) U_M \quad (\text{D2})$$

and a fourfold rotation symmetry, implemented by

$$H(k_x, k_y, k_z) = U_{\text{Rot}}^\dagger H(-k_y, k_x, k_z) U_{\text{Rot}}. \quad (\text{D3})$$

The mirror symmetry pins the red nodal line in Fig. 1 to the $k_z = 0$ plane, while the rotation symmetry pins the intersection points of the green and blue nodal line to the k_z axis.

We can understand the stability of the intersection points by first computing the winding numbers across an intersection—for instance the one between the red and the blue loop as shown in Fig. 24(a). We note that the winding number changes sign across the intersection. Consequently, the intersection can only be removed by splitting the nodal lines in the two ways shown in Figs. 24(b) and 24(c), while Fig. 24(d) is forbidden. On the other hand, the configurations shown in Figs. 24(b) and 24(c) are not compatible with the mirror symmetry mentioned above, because both require that the red nodal line leaves the $k_z = 0$ plane. Thus, as long as mirror symmetry remains intact, there is no possibility to remove any of the intersection points in the $k_z = 0$ plane. The intersection of the green and blue nodal line, on the other hand, is protected by the fourfold rotation symmetry around the z axis.

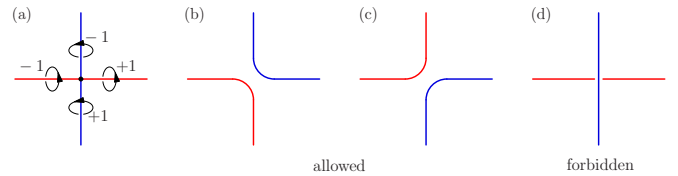


FIG. 24. (a) Intersection of two nodal lines in (8,3)n with corresponding winding numbers. There are only two splittings of the intersection that are compatible with the winding numbers, shown in (b) and (c), while the one in (d) is forbidden.

- [1] C. Herring, Accidental degeneracy in the energy bands of crystals, *Phys. Rev.* **52**, 365 (1937).
- [2] G. E. Volovik, *The Universe in a Helium Droplet* (Clarendon, Oxford, 2003).
- [3] G. E. Volovik, Quantum phase transitions from topology in momentum space, in *Quantum Analogues: From Phase Transitions to Black Holes and Cosmology*, edited by W. G. Unruh and R. Schützhold (Springer, Berlin Heidelberg, 2007), pp. 31–73.
- [4] X. Wan, A. M. Turner, A. Vishwanath, and S. Y. Savrasov, Topological semimetal and Fermi-arc surface states in the electronic structure of pyrochlore iridates, *Phys. Rev. B* **83**, 205101 (2011).
- [5] N. P. Armitage, E. J. Mele, and A. Vishwanath, Weyl and Dirac semimetals in three-dimensional solids, *Rev. Mod. Phys.* **90**, 015001 (2018).
- [6] A. A. Burkov, M. D. Hook, and L. Balents, Topological nodal semimetals, *Phys. Rev. B* **84**, 235126 (2011).
- [7] M. Phillips and V. Aji, Tunable line node semimetals, *Phys. Rev. B* **90**, 115111 (2014).
- [8] C.-K. Chiu and A. P. Schnyder, Classification of reflection-symmetry-protected topological semimetals and nodal superconductors, *Phys. Rev. B* **90**, 205136 (2014).
- [9] T. Bzdušek, Q. Wu, A. Rüegg, M. Sigrist, and A. A. Soluyanov, Nodal-chain metals, *Nature (London)* **538**, 75 (2016).
- [10] J.-W. Rhim and Y. B. Kim, Landau level quantization and almost flat modes in three-dimensional semimetals with nodal ring spectra, *Phys. Rev. B* **92**, 045126 (2015).
- [11] C. L. Kane and E. J. Mele, Z_2 Topological Order and the Quantum Spin Hall Effect, *Phys. Rev. Lett.* **95**, 146802 (2005).
- [12] B. A. Bernevig, T. L. Hughes, and S.-C. Zhang, Quantum spin Hall effect and topological phase transition in HgTe quantum wells, *Science* **314**, 1757 (2006).
- [13] J. E. Moore and L. Balents, Topological invariants of time-reversal-invariant band structures, *Phys. Rev. B* **75**, 121306 (2007).
- [14] L. Fu, C. L. Kane, and E. J. Mele, Topological Insulators in Three Dimensions, *Phys. Rev. Lett.* **98**, 106803 (2007).
- [15] R. Roy, Topological phases and the quantum spin Hall effect in three dimensions, *Phys. Rev. B* **79**, 195322 (2009).
- [16] M. König, S. Wiedmann, C. Brüne, A. Roth, H. Buhmann, L. W. Molenkamp, X.-L. Qi, and S.-C. Zhang, Quantum spin Hall insulator state in HgTe quantum wells, *Science* **318**, 766 (2007).
- [17] M. Z. Hasan and C. L. Kane, Colloquium: Topological insulators, *Rev. Mod. Phys.* **82**, 3045 (2010).
- [18] X.-L. Qi and S.-C. Zhang, Topological insulators and superconductors, *Rev. Mod. Phys.* **83**, 1057 (2011).
- [19] Y. Kim, B. J. Wieder, C. L. Kane, and A. M. Rappe, Dirac Line Nodes in Inversion-Symmetric Crystals, *Phys. Rev. Lett.* **115**, 036806 (2015).
- [20] C. Fang, Y. Chen, H.-Y. Kee, and L. Fu, Topological nodal line semimetals with and without spin-orbital coupling, *Phys. Rev. B* **92**, 081201 (2015).
- [21] Y.-H. Chan, C.-K. Chiu, M. Y. Chou, and A. P. Schnyder, Ca_3P_2 and other topological semimetals with line nodes and drumhead surface states, *Phys. Rev. B* **93**, 205132 (2016).
- [22] Y. X. Zhao and Z. D. Wang, Topological Classification and Stability of Fermi Surfaces, *Phys. Rev. Lett.* **110**, 240404 (2013).
- [23] A. Yamakage, Y. Yamakawa, Y. Tanaka, and Y. Okamoto, Line-node dirac semimetal and topological insulating phase in noncentrosymmetric pnictides CaAgX ($X = \text{P, As}$), *J. Phys. Soc. Jpn.* **85**, 013708 (2016).
- [24] B.-J. Yang, T. A. Bojesen, T. Morimoto, and A. Furusaki, Topological semimetals protected by off-centered symmetries in nonsymmorphic crystals, *Phys. Rev. B* **95**, 075135 (2017).
- [25] K. Mullen, B. Uchoa, and D. T. Glatzhofer, Line of Dirac Nodes in Hyperhoneycomb Lattices, *Phys. Rev. Lett.* **115**, 026403 (2015).
- [26] M. Ezawa, Loop-Nodal and Point-Nodal Semimetals in Three-Dimensional Honeycomb Lattices, *Phys. Rev. Lett.* **116**, 127202 (2016).
- [27] M. Tsuchiizu, Three-dimensional higher-spin Dirac and Weyl dispersions in the strongly isotropic K_4 crystal, *Phys. Rev. B* **94**, 195426 (2016).
- [28] K. O'Brien, M. Hermanns, and S. Trebst, Classification of gapless Z_2 spin liquids in three-dimensional Kitaev models, *Phys. Rev. B* **93**, 085101 (2016).
- [29] M. G. Yamada, V. Dwivedi, and M. Hermanns, Crystalline Kitaev spin liquids, *Phys. Rev. B* **96**, 155107 (2017).
- [30] H. Weng, Y. Liang, Q. Xu, R. Yu, Z. Fang, X. Dai, and Y. Kawazoe, Topological node-line semimetal in three-dimensional graphene networks, *Phys. Rev. B* **92**, 045108 (2015).
- [31] A. Mizuno, Y. Shuku, R. Suizu, M. M. Matsushita, M. Tsuchiizu, D. R. Maneru, F. Illas, V. Robert, and K. Awaga, Discovery of the K_4 structure formed by a triangular π radical anion, *J. Am. Chem. Soc.* **137**, 7612 (2015).
- [32] A. Mizuno, Y. Shuku, M. M. Matsushita, M. Tsuchiizu, Y. Hara, N. Wada, Y. Shimizu, and K. Awaga, 3D Spin-Liquid State in an Organic Hyperkagome Lattice of Mott Dimers, *Phys. Rev. Lett.* **119**, 057201 (2017).
- [33] T. Takayama, A. Kato, R. Dinnebier, J. Nuss, H. Kono, L. S. I. Veiga, G. Fabbri, D. Haskel, and H. Takagi, Hyperhoneycomb Iridate $\beta\text{-Li}_2\text{IrO}_3$ as a Platform for Kitaev Magnetism, *Phys. Rev. Lett.* **114**, 077202 (2015).
- [34] K. A. Modic, T. E. Smidt, I. Kimchi, N. P. Breznay, A. Biffin, S. Choi, R. D. Johnson, R. Coldea, P. Watkins-Curry, G. T. McCandless, J. Y. Chan, F. Gandara, Z. Islam, A. Vishwanath, A. Shekhter, R. D. McDonald, and J. G. Analytis, Realization of a three-dimensional spin-anisotropic harmonic honeycomb iridate, *Nat. Commun.* **5**, 4203 (2014).
- [35] M. G. Yamada, H. Fujita, and M. Oshikawa, Designing Kitaev Spin Liquids in Metal-Organic Frameworks, *Phys. Rev. Lett.* **119**, 057202 (2017).
- [36] A. F. Wells, *Three-Dimensional Nets and Polyhedra* (Wiley, New York, 1977).
- [37] M. Hermanns and S. Trebst, Quantum spin liquid with a Majorana Fermi surface on the three-dimensional hyperoctagon lattice, *Phys. Rev. B* **89**, 235102 (2014).
- [38] H. Heesch and F. Laves, Über dünne Kugelpackungen, *Z. Kristallogr.* **85**, 443 (1993).
- [39] T. Sunada, Crystals That Nature Might Miss Creating, *Notices of the AMS* **55**, 208 (2008).
- [40] Note that for the lattices (10,3)a, (8,3)a, and (8,3)b sublattice symmetry comes with a nonzero momentum \vec{k}_0 and therefore the product PS of time-reversal and sublattice symmetry is *not*

- momentum invariant. It is for this reason that these lattices do not exhibit nodal lines.
- [41] A. Altland and M. R. Zirnbauer, Nonstandard symmetry classes in mesoscopic normal-superconducting hybrid structures, *Phys. Rev. B* **55**, 1142 (1997).
- [42] G. Li and E. Y. Andrei, Observation of Landau levels of Dirac fermions in graphite, *Nat. Phys.* **3**, 623 (2007).
- [43] We implement the magnetic field by assigning the phase $\phi = \pm n\pi\phi_F/\phi_{\text{tot}}$ to the z bonds (see also the next reference), with $n\vec{a}_y$ denoting the y position of the unit cell and ϕ_{tot} denoting the total flux. This assigns a flux 2ϕ to all the plaquettes that are penetrated by the magnetic field. Since we want to describe arbitrary flux through the plaquette, we use open boundary conditions in the y direction. Note that k_y is no longer a good quantum number.
- [44] To facilitate our analysis we work with the most symmetric representation of the (10,3)b hyperhoneycomb lattice. In this representation the elementary zigzag chains constituting the lattice, see Fig. 2, are rotated by 90° with respect to each other. We further double the unit cell, see Appendix A, which allows us to choose orthogonal lattice translation vectors (as compared with the minimal representation of the lattice). With these conventions the nodal line lies in the (k_x, k_y) plane, see also Fig. 17 in Appendix A.
- [45] E. McCann and V. I. Fal'ko, Landau-Level Degeneracy and Quantum Hall Effect in a Graphite Bilayer, *Phys. Rev. Lett.* **96**, 086805 (2006).
- [46] H. Nielsen and M. Ninomiya, Absence of neutrinos on a lattice: (II). Intuitive topological proof, *Nucl. Phys. B* **193**, 173 (1981).
- [47] H. Nielsen and M. Ninomiya, Absence of neutrinos on a lattice: (I). Proof by homotopy theory, *Nucl. Phys. B* **185**, 20 (1981).
- [48] B. Bradlyn, J. Cano, Z. Wang, M. G. Vergniory, C. Felser, R. J. Cava, and B. A. Bernevig, Beyond Dirac and Weyl fermions: Unconventional quasiparticles in conventional crystals, *Science* **353**, 5037 (2016).
- [49] H. Watanabe, Y. Hatsugai, and H. Aoki, Manipulation of the Dirac cones and the anomaly in the graphene related quantum Hall effect, *J. Phys.: Conf. Series* **334**, 012044 (2011).
- [50] J. D. Malcolm and E. J. Nicol, Magneto-optics of general pseudospin- s two-dimensional Dirac-Weyl fermions, *Phys. Rev. B* **90**, 035405 (2014).
- [51] M. Orlita, D. M. Basko, M. S. Zholudev, F. Teppe, W. Knap, V. I. Gavrilenko, N. N. Mikhailov, S. A. Dvoretiskii, P. Neugebauer, C. Faugeras, A.-L. Barra, G. Martinez, and M. Potemski, Observation of three-dimensional massless Kane fermions in a zinc-blende crystal, *Nat. Phys.* **10**, 233 (2014).
- [52] I. C. Fulga and A. Stern, Triple point fermions in a minimal symmorphic model, *Phys. Rev. B* **95**, 241116 (2017).
- [53] M. Hermanns, K. O'Brien, and S. Trebst, Weyl Spin Liquids, *Phys. Rev. Lett.* **114**, 157202 (2015).
- [54] A. P. Schnyder, P. M. R. Brydon, and C. Timm, Types of topological surface states in nodal noncentrosymmetric superconductors, *Phys. Rev. B* **85**, 024522 (2012).
- [55] A. Mook, J. Henk, and I. Mertig, Magnon nodal-line semimetals and drumhead surface states in anisotropic pyrochlore ferromagnets, *Phys. Rev. B* **95**, 014418 (2017).
- [56] S. Trebst, Kitaev Materials, [arXiv:1701.07056](https://arxiv.org/abs/1701.07056).
- [57] Note that the (8,3)a lattice shown in Fig. 2 has counterclockwise rotating spirals.